

Johnson Matthey's international journal of research exploring science and technology in industrial applications

\*\*\*\*\*Accepted Manuscript\*\*\*\*\*

## This article is an accepted manuscript

It has been peer reviewed and accepted for publication but has not yet been copyedited, house styled, proofread or typeset. The final published version may contain differences as a result of the above procedures

It will be published in the **January 2023** issue of the *Johnson Matthey Technology Review*

Please visit the website <https://technology.matthey.com/> for Open Access to the article and the full issue once published

## Editorial team

**Manager** Dan Carter

**Editor** Sara Coles

**Editorial Assistant** Yasmin Stephens

**Senior Information Officer** Elisabeth Riley

Johnson Matthey Technology Review

Johnson Matthey Plc

Orchard Road

Royston

SG8 5HE

UK

**Tel** +44 (0)1763 253 000

**Email** [tech.review@matthey.com](mailto:tech.review@matthey.com)



## X-ray Computed Tomography for Failure Mechanism Characterisation within Layered Pouch Cells

Drasti Patel<sup>1</sup>, Hamish Reid<sup>1</sup>, Sarah Ball<sup>2</sup>, Dan J.L. Brett<sup>1,3</sup>, and Paul R. Shearing<sup>1,3</sup>

<sup>1</sup>Electrochemical Innovation Lab, Department of Chemical Engineering, University College London, London, WC1E 7JE, UK

<sup>2</sup>Johnson Matthey Battery Materials, 142A Park Drive, Milton Park, Abingdon, OX14 4SE, UK

<sup>3</sup>The Faraday Institution, Quad One, Becquerel Avenue, Harwell Campus, Didcot, OX11 0RA, UK

Web: [www.ucl.ac.uk/electrochemical-innovation-lab](http://www.ucl.ac.uk/electrochemical-innovation-lab)

Email: [p.shearing@ucl.ac.uk](mailto:p.shearing@ucl.ac.uk)

<Article history>

PEER REVIEWED

Submitted 28th February 2022; Revised 8th July 2022; Accepted 2nd August 2022;

Online 3rd August 2022

<End of article history>

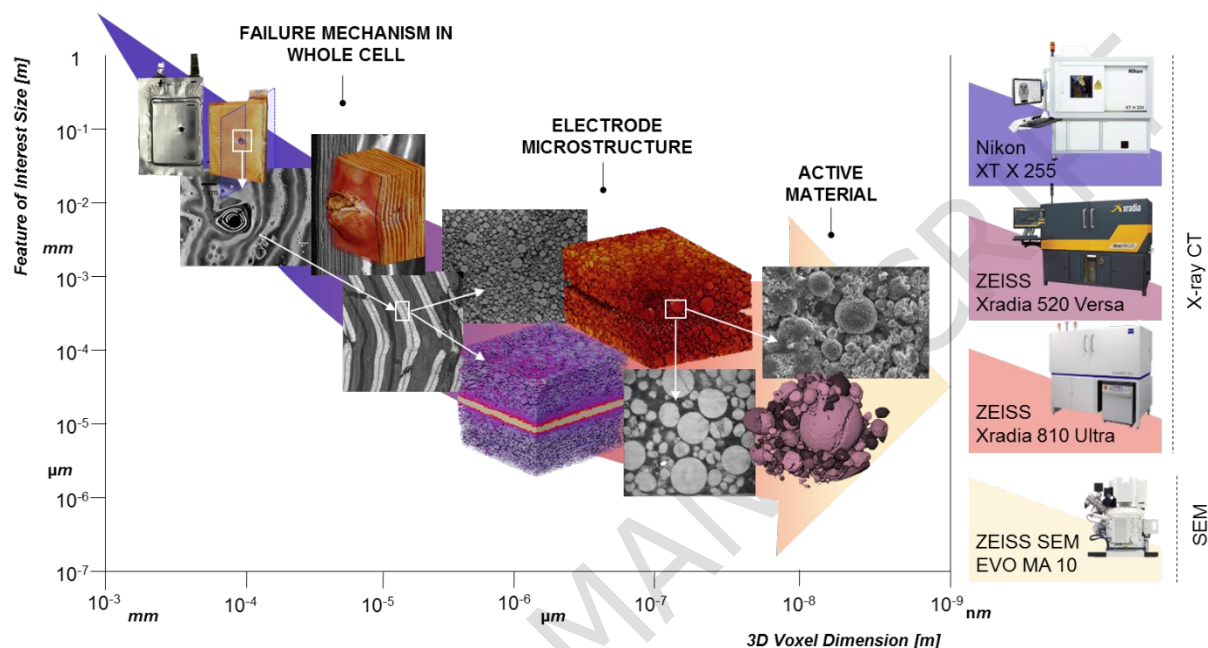
### Abstract

Lithium-ion battery (LIB) safety is a multi-scale problem: from the whole-cell architecture to its composite internal 3D microstructures. Substantial research is required to standardise failure assessments and optimise cell designs to reduce the risks of LIB failure. In this work, the failure response of a 1 Ah layered pouch cell with a commercially available NMC cathode and graphite anode at 100 % SOC (4.2 V) is investigated. The mechanisms of two abuse methods; mechanical (by nail penetration) and thermal (by accelerating rate calorimetry) are compared by using a suite of post-mortem analysis methods.

Post-mortem whole-cell architectural changes and electrode layer deformations were analysed for both mechanisms using non-invasive X-ray computed tomography. Furthermore, changes to electrode surfaces, bulk microstructures and particle

morphologies are compared by following a proposed cell disassembly and post-mortem sample preparation methodology. Building on the insights into critical architectural weak points, electrode behaviours and particle cracks, the reliability of X-ray computed tomography as a guide for LIB failure assessment is demonstrated.

## Graphical Abstract



## Keywords

Lithium-ion battery; Pouch cell; Nail penetration; Thermal runaway; Post-mortem analysis; Cell disassembly; X-ray computed tomography; Multi-length scale imaging

## 1 Introduction

### 1.1 Lithium-ion battery (LIB) failure

The lithium-ion battery (LIB) is a key technology for the future of energy storage. Its high power, long cycle life, and high specific energy alongside its decreasing manufacturing cost make it the electrochemical technology of choice for sustainable mobility and renewable energy implementation(1)(2). Concerns regarding LIB safety, however, continue to be prevalent in their widespread application(3). During operation outside of their normal (or safe) operating window, LIBs can ignite and initiate fires or release toxic gases(4). Although statistically rare(5), some LIB failures are heavily

publicised: firstly due to the speed at which they're becoming a ubiquitous technology in modern society, but also because of their unique failure behaviour in terms of initiation, spread, and duration when compared to other fire hazards(6). An example of LIB safety in the media is a product recall by Sony in 2006 of 9.6 million LIBs powering laptops of well-known computer manufacturers(7) that were deemed fire hazards due to faulty crimping and the introduction of microscopic metal contaminants during manufacture. Similarly, ten years later, Samsung recalled 2.5 million Note 7 mobile phones(8) because of the use of thinner than normal separators and poor alignment of components(9). More recent headlines include fires within electric vehicles (EVs) such as several Tesla Model S cars between 2013 – 2021(10)(11) and a Jaguar I-Pace in 2021(12). China, one of the world's largest markets for EVs reports sudden ignition due to contaminants and charging as the main causes of LIB fires in EVs(13). These events highlight the numerous variables that shape a battery safety incident; from the cause of failure, application type, and therefore battery format, management system, and extent of the damage.

The mechanical integrity and heat dissipation of cells are important when considering LIB safety. The four most commonly used LIB formats are cylindrical, prismatic, coin/button or pouch. Prismatic cells generally have larger capacities than cylindrical, so fewer cells need to be connected in a pack for the desired capacity. Coin or button cells are small and typically used for laboratory-scale materials testing. Pouch cells offer greater flexibility in terms of matching the cell to a specific device shape(14). Within all of these formats, aside from the highly oxidising and reducing electrode materials (anode and cathode), the likelihood of failure and/or severity of an event is compounded by poor heat dissipation(3). The higher capacities of prismatic cells make it more difficult to dissipate heat(15) and make cooling more challenging, while the smaller physical size of cylindrical cells makes it easier to assemble them into packs (e.g. with gaps between cells) to improve overall heat dissipation. Prismatic and cylindrical cells have metallic outer shell casings that can withstand high pressure, whereas pouch cells are cased in aluminium-plastic composite films which make them more susceptible to deformations such as piercing, bulging or swelling. Furthermore, LIBs are composite systems made up of active particles, liquid electrolytes, metallic current collectors and separators, all of which should be addressed at each scale when assessing battery safety(3)(16).

Figure 1 illustrates the possible scenarios and outcomes of LIB failure. In cases where heat generation is not controlled, elevated temperatures may trigger a series of undesirable exothermic reactions that could sustain themselves enough to cause ruptures, venting of gases, explosions and/or eventually lead to fires (i.e. thermal runaway (TR)). The response of a LIB in situations where mechanical damage to shell casings (punctures or compression), electrical (overcharge/discharge or short circuit), or thermal damage (local heating) has occurred will vary depending on the format of the cell and its integrated battery management system (BMS), its capacity and its chemistry(17). Therefore, an effective strategy to interpret LIB safety and reduce the number of failure events is to characterise features across these multiple scales: from the whole-cell architecture to its individual components.

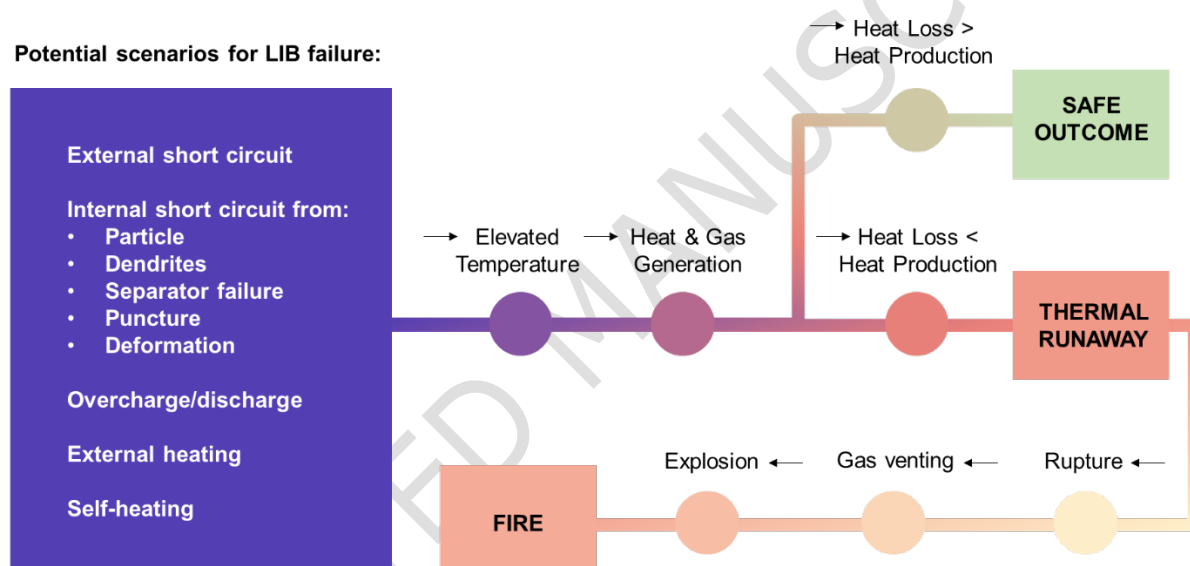


Figure 1 Flowchart depicting the possible outcomes of a typical lithium-ion battery failure sequence adapted from Total Battery Consulting(18).

## 1.2 Investigation of LIB safety

Manufacturers, organisations, and battery researchers investigate and characterise the various mechanisms related to LIB safety by deliberately creating scenarios that may trigger thermal runaway (TR). A test set-up can involve overcharge/discharge, heating, short circuit, internal short circuit, nail penetration, or crushing. Despite standardisation efforts across these, current LIB safety testing standards have different guidelines for each. Table 1 summarises two methods (heating and nail penetration) used to trigger battery failure in five selected safety testing standards adapted from Chen et al(16).

Heating tests are used to analyse the LIBs' thermal stability and heat distribution. GB/T31485 deems a battery as 'safe' if it does not leak or combust after it is placed in a hot box and heated to 130 °C at 5 °C min<sup>-1</sup> and kept at this temperature for 30 min. Nail penetration tests are designed to simulate an internal short circuit (ISC) that may occur when the internal components are penetrated with impurities. An ISC event generates large quantities of local heat which may lead to TR. According to GB/T31485, the battery should be at 100 % SOC before it is penetrated by a high-temperature resistant stainless steel nail (with a diameter between 5 – 8 mm) at a speed of 25 mm s<sup>-1</sup>. The penetration position should also be as close to the geometrical centre of the cell and the nail should reach 100 % of the depth of the battery.

Several research efforts have been made to compare the results of varying the battery state-of-charge (SOC) and capacity when heating as well as the depth and position of the nail during penetration tests. For example, Mendoza-Hernandez et al. report that TR is triggered much sooner and at a lower onset temperature in a cell at 100% SOC compared to 50 % SOC(19). The severity of reactions is reported to be greater when a cylindrical cell is penetrated at the centre as opposed to the top and bottom, while higher nail penetration speeds decreased the uniformity of temperature distribution within the cell(20). Therefore, it is crucial to consider how such variations can affect the extent of failure and interpretation of LIB safety.

*Table 1 Summary of heating and nail penetration testing guidelines from five selected safety testing standards adapted from Chen et al.(16)*

Trigger mechanism for battery failure	Safety testing standard				
	GB/T31485-2015	IEC62133	SAE J2464	VW PV8450	USABC-GM
Heating	Heating at 5 °C min <sup>-1</sup> from 25 °C to 130 °C, hold for 30 min	130 °C, 10 min	Max. stable temperature	2 °C min <sup>-1</sup> to 130 °C or 200 °C hold for 30 min	0.5 °C min, 50-150 °C, hold for 30 min
Nail penetration	Penetration rate: 25 mm/s, diameter: 5 -	N/A	80 mm/s, diameter: 3	0.1 mm/s, diameter: 1mm stainless	80 mm/s, diameter: 3 mm, 100% depth

8mm, 100%  
depth

mm, 100%  
depth

steel, 2 mm  
depth

---

### 1.3 Thermal analysis

In a comprehensive review of LIB fire safety studies, Ruiz et al. report that most literature focuses on single cell and component scales as opposed to module or pack scales(21). The failure behaviour of larger scale battery packs is different to individual cells and so the outcome of investigations also differs depending on the scale at which they are studied. Investigations can therefore be categorised by order of 'layer of protection' starting from prevention, compartmentation, and detection to suppression of the fire(21). The prevention layer aims to avoid the failure scenario altogether and is the category for most single cell and component scale investigations. For this, the fundamental mechanisms that trigger and sustain the failure need to be understood; which is also where the focus of the current work lies.

Many studies have analysed the behaviour of LIBs at elevated temperatures and a set of key characteristic reactions during failure have been established(22). Adiabatic calorimetry (e.g. accelerating rate calorimetry (ARC) and differential scanning calorimetry (DSC)) have been used to investigate the decomposition of materials as individual components as well as components within a complete cell(23)(24)(25)(26). It is generally known that once initiated (by a high temperature), a series of exothermic reactions will begin. First is the decomposition of the solid electrolyte interphase (SEI) layer typically between 60 – 100 °C(17). This is a thin passivating layer that forms across the electrode layer surface and its decomposition generates gas and leaves the active electrode surface exposed to electrolyte. Intercalated lithium on the anode reacts with the electrolyte and further heat and gas is generated. As the temperature of the cell increases, the cathode layer becomes unstable and begins to decompose(27). Furthermore, the overpressure within the cell may cause the outer casing of the cell to break or rupture. The introduction of oxygen to the system creates a flammable mixture and combustion reactions may follow (causing flames and fires)(28).

This reaction series and its associated kinetic parameters has been extensively modelled to understand and predict thermal runaway(29)(30)(31). The effects of cell

geometry and configuration were studied by Lopez et al. who found that a prismatic shape had a slower temperature response and failure reaction kinetics than a cylindrical shape(32). Several models exist for thermal runaway triggered by various mechanical loadings and crash events, however, Zhu et al. concludes that due to the inhomogeneity between the numerous behaviours such as temperature, pressure-dependence, anisotropy, or ductile fracture, each component (current collector, coating, separator, shell casing) exhibits, models are currently limited to the microscale(33).

#### 1.4 Image analysis

When attempting to understand the evolution of a particular failure mechanism within a LIB, it is important to consider the method by which the failed batteries are examined. Waldmann et al. reviews state-of-art methods by which aged cells are disassembled including microscopy, various chemical methods which are sensitive to electrode surfaces and reconstruction of electrodes into half and full cells(34). However, each method only observes a specific aspect of a LIB material behaviour making it difficult to characterise failure mechanisms using only electrochemical and physicochemical measurements of single materials(35). Imaging techniques such as SEM(36), X-ray radiography(37)(38)(39), X-ray CT(40)(41)(42) and neutron tomography(43) have been proven to be useful complementary methods to obtain visual observations of materials during and after a failure incident.

Mao et al. compare the anode extracted from a cylindrically wound cell after nail penetration with that of a pristine graphite anode and finds that the layered structure is still intact but has some additional fragments and voids where flammable materials may have been consumed by the TR reactions(20). Micro-CT was used in combination with XRD by Zhang et al. to visualise the cross-section of a jelly-roll pouch cell. A buckling behaviour was observed at the folded edges of the electrode layers as a function of extreme cycling. Ripples created by this posed a high chance of ISCs. As a result, the authors proposed optimised anode layer structures that controlled the distribution of stress and constraint in a jelly-roll cell(44).

The impact of low-temperature charging on the degradation of LIB materials was conducted by We et al. using a cell-opening method where the jelly-roll structure was unwound and separated into cathode, anode and separator. They were visually



inspected for surface smoothness, detachment of active material and regions of exfoliation from the current collectors. Lithium plating on the anode was observed, and later SEM scans revealed cracks between primary particles when compared with fresh cell materials(45).

Finegan et al. investigated the effects of overcharge-induced thermal runaway on LIB materials using *operando* X-ray CT. A post-mortem multi-scale approach was introduced whereby significant morphological and phase changes in a LiCoO<sub>2</sub> pouch cell after failure were examined using X-ray CT at the whole cell, bulk electrode structure and particle scales. The post-mortem battery architecture, bulk electrode, and particle degradation revealed how failure mechanisms propagated across multiple spatial resolutions(46).

As demonstrated by literature, X-ray CT for post-failure analysis is predominantly used to see where failure-causing defects are located(47) and/or to assess where samples should be extracted from upon cell opening for further analysis(35). However, X-ray CT offers a wide range of imaging capabilities across multiple length scales that are often scattered in their application or approach and largely underused when characterising LIB failure. This work aims to combine some of the existing X-ray CT imaging methods for battery materials and introduces a step-by-step procedure for post-failure analysis of LIBs that involves whole-cell imaging, cell-opening and material extraction. Furthermore, the results obtained from sample preparation techniques that are non-invasive and invasive are compared regarding representativeness. Investigations are carried out for two different failure triggers (a thermally failed and a nail penetrated cell) which provide a range of characteristic failure features such as swelling, rupture, or cracking. As a result, the whole-cell architecture and electrode deformations can be compared against a pristine cell and for each failure mechanism. Additionally, the failure mechanisms are discussed from a failure prevention perspective, i.e. finding the mechanisms by which Joule heating and/or material decomposition occurs and how they can be mitigated: by controlling heat generation and enhancing heat dissipation within a pouch cell. This work addresses the challenge of consistency across existing LIB failure characterisation. Overall, the benefits of X-ray CT to aid the design, manufacture and use of LIBs in ways that can mitigate known safety hazards are demonstrated.

## 2 Experimental and methodology

This study combined battery failure testing with imaging to develop a guide for post-failure LIB analysis. The method followed a step-by-step investigation where failed cells were initially inspected as a whole, by eye and using X-ray CT for large characteristic features such as pouch swelling and later opened up to extract materials for investigations using micro- and nanoscale X-ray CT. Investigations at smaller length scales provided an insight into the effects of battery failure on bulk and individual particles. Features such as particle cracking and the extent to which contaminants penetrated the electrode layer particles could be determined. Three 1 Ah layered lithium-ion batteries with a pouch cell format were tested for their response to two battery failure trigger modes. One cell was assigned as the control (Cell 1), and the remaining cells were investigated under external heating (Cell 2) and nail penetration (Cell 3), respectively. Details of the failure methods and measurements are described in *2.2 Battery failure methods and measurements*. All cell samples consisted of twenty one double-sided electrode layers, with ten positive electrodes, denoted as the cathode, and eleven negative electrodes (graphite) denoted as the anode. The cathode material, lithium nickel manganese cobalt oxide (NMC811), was sourced from Targray, Canada. The electrochemical properties and assigned failure modes for each cell are summarised in Table 2.

### 2.1 Cell fabrication and electrochemical characterisation

The electrode processing, drying and cell assembly were all carried out at QinetiQ Ltd on behalf of Johnson Matthey Battery Materials using commercially available materials. The cells were assembled inside a dry room with a  $-40^{\circ}\text{C}$  dew point. For fabrication of pouch cells, electrodes with  $36.5 \times 49.0$  mm dimension (electrode area =  $17.885 \text{ cm}^2$ ) with an additional uncoated tab area were punched from laminated double-sided sheets. Pouch cells were assembled with ten cathode and eleven anode layers, giving a total active area of  $357.7 \text{ cm}^2$ . The cathode was deposited on an Al current collector with a thickness of  $15 \mu\text{m}$  and the anode was deposited on a Cu current collector with a thickness of  $10 \mu\text{m}$ .

The electrochemical performance of the pouch cells was tested in a two-electrode configuration using either a Bio-logic VMP3 (Seyssinet-Pariset 38170, France) or Arbin MSTAT 8000 (TX 77845, USA) battery cycler. The cells underwent a

constant-current constant-voltage (CCCV) formation protocol with three cycles between 2.7 V and 4.2 C using a C-rate of C/10 at 21 °C. A current cut-off of 0.05 C was used for the constant voltage step. The specific capacity and current density were measured with respect to the mass of the active material.

Table 2 Summary of samples, electrochemical properties and assigned failure modes.

Sample code	Anode nominal capacity/ Ah	Cathode nominal capacity/ Ah	Ratio $Q_{an}/Q_{cath}$ per 4.3 V	Specific capacity/ mAh/g	Specific energy/ Wh/kg	Cell failure mode
Cell 1	1.418	1.206	1.16	193.7	215.0	Pristine cell (no failure mode)
Cell 2	1.426	1.215	1.16	195.7	218.2	External heating by accelerating rate calorimetry (ARC)
Cell 3	1.438	1.215	1.17	194.7	216.7	Internal short circuit (ISC) by nail penetration

## 2.2 Battery failure methods and measurements

### *Thermal: External heating by ARC*

Accelerating rate calorimetry (ARC) was used to determine the onset temperature for thermal runaway and the rate of heat generation within Cell 2 during failure. The pouch cell was cycled by a CCCV protocol conducted at 1 C constant current, from 3.0 – 4.2 V, and using a constant voltage protocol until the current cut-off of 0.05 C. Before conducting the ARC experiments, the OCV was checked to ensure no voltage drop had occurred. The cell was heated up using ARC inside an adiabatic chamber (Phitec Battery Test Calorimeter, HEL Group, Herts., UK) with a heat-wait-search (HWS) protocol. Two thermocouples were attached to the bottom and top of the cell as close to the centre as possible. A heating coil was wound around the sample and secured using aluminium tape and the thermocouples were secured using glass fibre tape. A photograph of the cell set up inside the calorimeter is shown in Figure S1. Once the cell had reached a start temperature of 50 °C, HWS was initiated. After which, the calorimeter increased the temperature in discrete steps of 5 °C and monitored the cell temperature for 5 min. If in this time the temperature

remained unchanged, up to a threshold value, approximately  $0.02\text{ }^{\circ}\text{C min}^{-1}$ , the calorimeter then continued to increase the temperature by  $5\text{ }^{\circ}\text{C}$  until self-heating was detected(40).

### *Mechanical: Internal short circuit (ISC) by nail penetration*

The nail penetration test on Cell 3 was conducted using a battery penetration instrument (Pneumatic Nail Penetration Tester, MSK-800-TE9002, MTI Corp. CA, USA). The instrument is a large fire-proof chamber fitted with an air vent, clamps to hold the sample in place and a stainless steel nail with a 4 mm diameter. The pouch cell was fully charged to the maximum rated voltage, 4.2 V at 1 C using a CCCV charging protocol and was mounted horizontally. The nail was positioned so it would penetrate the centre of the cell and the penetration depth was chosen to fully pierce through all the layers at a speed of approximately  $30\text{ mm s}^{-1}$ . After penetration, the nail was slowly reversed out of the cell. Heat and voltage measurements were not recorded for this cell during failure. The behaviour of the cell was monitored by video and is available in (Cell 3\_Nail Penetration.mp4).

## **2.3 Imaging**

Tomographic reconstructions of multiple samples were produced using three lab-based X-ray CT systems: Nikon XT 225 (Nikon, Tring, UK), ZEISS Xradia 520 Versa and, ZEISS Xradia Ultra (Carl Zeiss XRM, Pleasanton, CA, USA). Whole battery scans, (i.e. without cell disassembly) are defined as 'non-invasive' and battery component scans, for imaging bulk electrode layers and particles, are defined as 'invasive'. For the latter, the battery was carefully dismantled and photographed during each stage of disassembly for sample collection. Sample preparation methods for invasive X-ray CT scans are outlined in Section 2.4: Post-mortem sample preparation. The features of interest, spatial resolution and imaging instrument used are categorised by the sample preparation method (invasive or non-invasive) and shown in Figure 2.

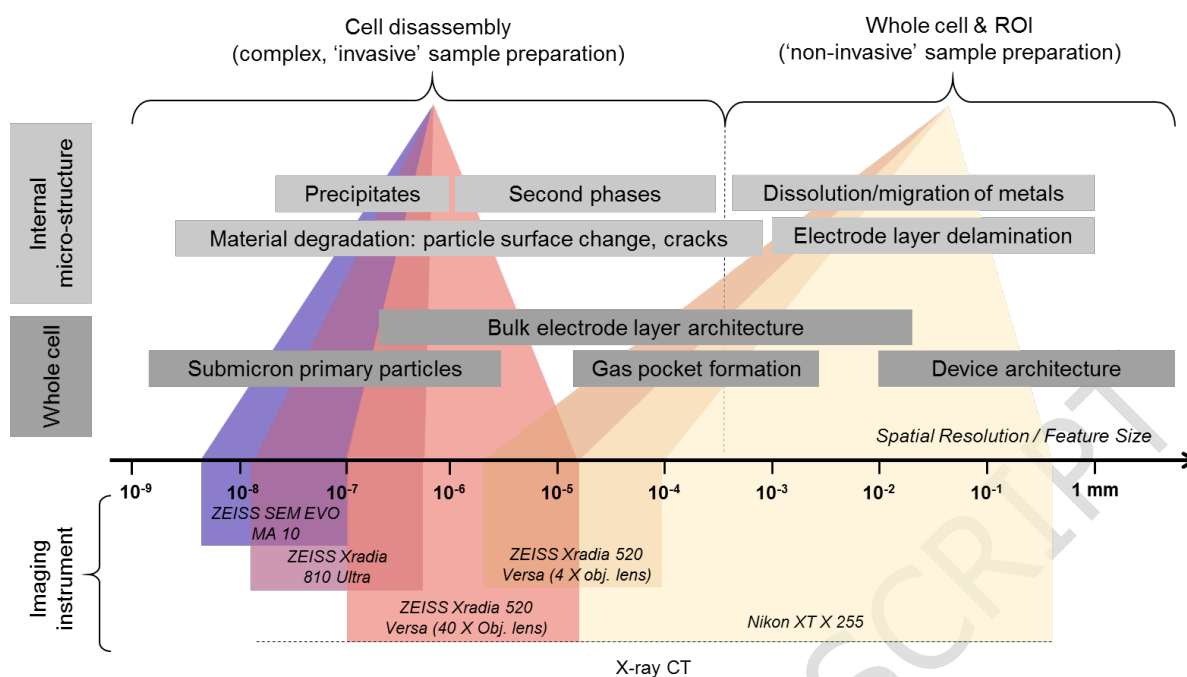


Figure 2 Imaging instruments (Scanning electron microscopy, SEM and X-ray Computed Tomography, X-ray CT) grouped for the type of sample preparation (invasive and non-invasive) required for the feature of interest/spatial resolution (adapted from Salvo et al.(48)).

For whole cell and region-of-interest (ROI), non-invasive scans, images were obtained using the Nikon XT 225 (Nikon) and the ZEISS Xradia 520 Versa (Versa) with a 4 X objective lens, respectively. For the Nikon, an accelerating voltage of 210 kV was used with a tungsten target to generate 3176 projections for each of the datasets acquired. The datasets were subsequently reconstructed using CT Pro 3D software with a built-in filtered back projection algorithm. The acquired datasets had voxel sizes ranging from 27.8 – 33.6  $\mu\text{m}$ . For the ROI datasets, a pixel binning of 1 was used and the voltage, exposure times, and number of projections were all varied for the sample type. The acquired pixel sizes are summarised in Table S1.

After opening the failed cells, samples were prepared according to the feature of interest as outlined in 2.4 Post-mortem sample preparation. The bulk electrode layer datasets were obtained using the ZEISS Xradia 520 Versa with a 40 X objective lens. Datasets for the thermally failed (Cell 2) and nail penetrated (Cell 3) cathode samples were obtained using a pixel binning of 2, a voltage of 80 kV, and an exposure time of 5 s, while the anode datasets were obtained using a lower voltage at 60 kV while all other parameters remained the same. The acquired pixel sizes are summarised in Table S1.

High resolution images of the cathodes extracted from all three cells were obtained using the ZEISS Xradia Ultra 810 with a fixed energy 5.4 keV, quasi-monochromatic beam. A voxel size of 0.0631  $\mu\text{m}$  was achieved for the pristine cathode and 0.126  $\mu\text{m}$  for the post failure cathode samples.

All SEM micrographs were obtained using the Zeiss EVO 10 SEM instrument. An SE1 signal was used at a 15 kV accelerating voltage and approximate magnifications ranging from 3,300 – 8,500, yielding pixel sizes between 35 – 90 nm for all images.

### *Image processing*

Reconstructed X-ray CT data was visualised using Avizo Fire 9.2 (FEI Company, Hillsboro, OR, USA). For all datasets, a non-local means filter was applied to reduce noise and preserve phase boundaries. This procedure was performed to prepare the datasets for threshold-based binarisation. Phases were separated based on their grey scale values where weakly attenuating materials are displayed in shades of grey (such as the separator, graphite anode and aluminium current collector) and highly attenuating materials (such as the cathode active material and copper current collector) in white. Voxels in the bulk electrode layer and particle scans were assigned to a particle or pore phase based on the measured grayscale value. The resulting binary images were used for measurements of porosity and PSD using the Avizo Fire 9.2 label analysis tool. Tortuosity factors and representative volume analyses were extracted using TauFactor, an open source MATLAB plugin, details of which are described in ref(49).

## **2.4 Post-mortem sample preparation**

Two methods were used to prepare the samples for the battery component (bulk electrode layer and particle morphology) analysis. Cells were left overnight in their respective instruments after failure for gases to safely dissipate. Once the cells had cooled to room temperature, they were imaged first via X-ray CT for the whole cell and ROI analysis. The cells were stored in air and later taken apart inside of a fume hood. For both cells, a scalpel was used to create an incision lengthwise at the side of the cell where the pouch had been vacuum sealed. The outer casing of the pouch was

peeled away carefully without disrupting the electrode layers as shown in Figures 3 (a)(i) and (b)(i). The electrode layer stack was removed first from within the cell casing by cutting the anode and cathode tabs. For the thermally failed cell (Cell 2), the central anode and cathode layers were removed and a 1 cm x 1 cm square from the centre of the electrodes was removed for further preparation (as shown in Figure 3 (a)(ii-iii) and (b)(ii-iii)). For the nail penetrated cell (Cell 3), the central anode and cathode layers were removed and the separator was carefully peeled off their surfaces. 1 cm x 1 cm squares were cut from the centre of both electrodes of this cell and subsequently used for 2D imaging via SEM. For 3D imaging via X-ray CT, the samples were processed further using a high precision laser, details of which follow.

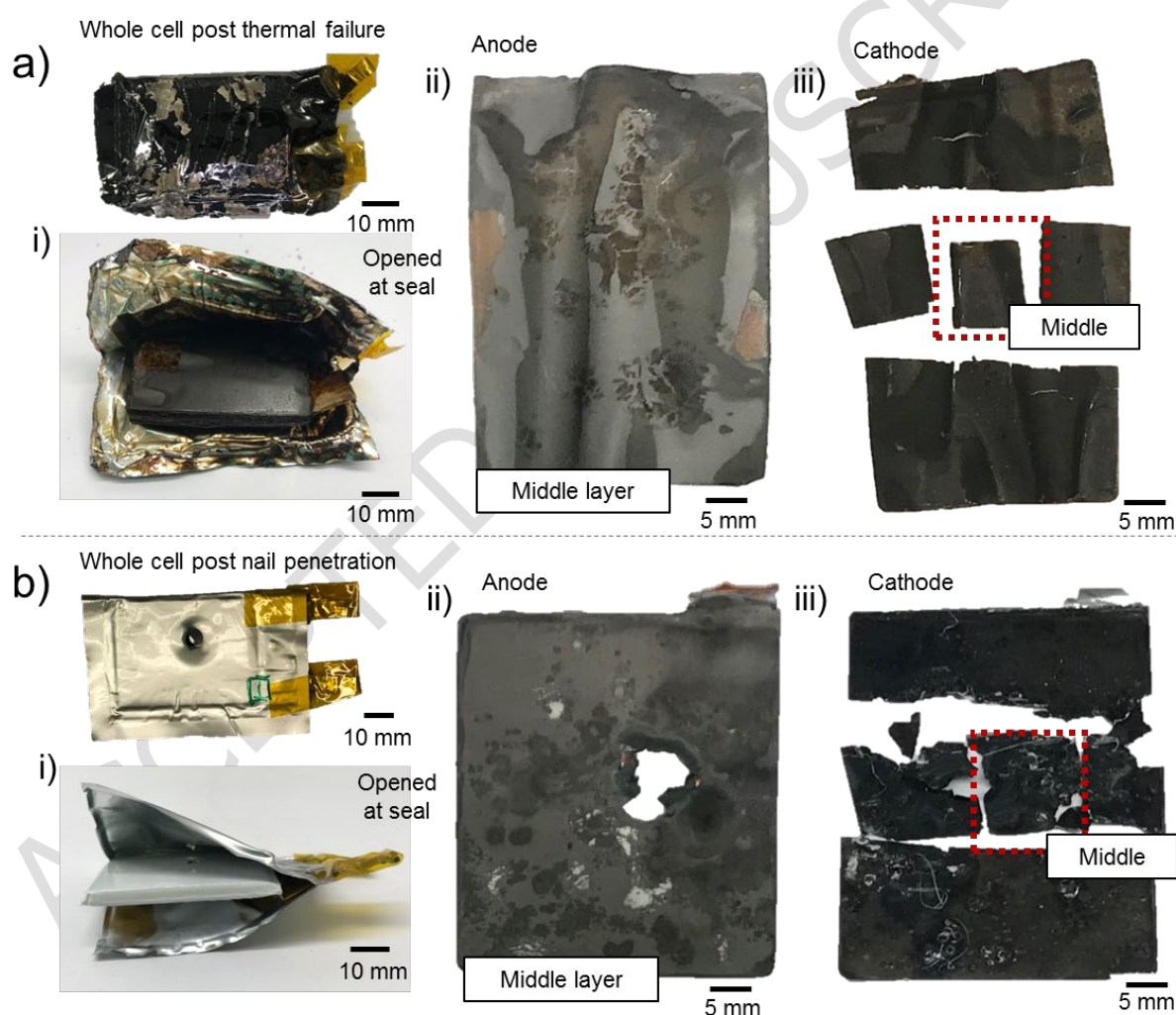


Figure 3 Photographs showing the disassembly of (a) the thermally failed cell (Cell 2) and (b) the nail penetrated cell (Cell 3). The aluminium-plastic composite casing was carefully cut at the vacuum sealed edge and peeled away in (a-b)(i). The central anode layer is shown in (a-b)(ii) and the central cathode layer is shown in (a-b)(iii) as well as where the samples for SEM and X-ray CT were extracted from.

Samples intended for 3D images of the bulk electrode were prepared by cutting 0.4 mm by 0.4 mm squares which were mounted onto a 3D printed stacker using Kapton tape. The samples fitted within the field-of-view (FOV) of the 40 X objective lens, ca. 400  $\mu\text{m}$ , in the X-ray micro-CT instrument (Zeiss Xradia 520 Versa, Carl Zeiss XRM, Pleasanton, CA, USA) and were held upright in a 3D printed stacker (Figure S2) to reduce the overall signal-to-noise ratio and scan time. This method produced 3D images with a 0.387  $\mu\text{m}$  voxel size of the four bulk electrode layers (anode and cathode each after thermal failure and nail penetration).

Samples intended for imaging at nano-scale resolutions to resolve individual particles (using the Zeiss Xradia Ultra 810) were prepared using a laser lathing micromachining technique (A Series/Compact Class 4 532 nm Laser Micromachining System, Oxford Lasers, Oxford, UK) as described by Bailey et al. (50). Small disks of 1 mm diameter were cut from the bulk electrode layers, glued to a pin and milled down to a diameter < 65  $\mu\text{m}$ . All samples were imaged in the large field of view (LFOV) absorption mode with a 65  $\mu\text{m}$  FOV.

### 3 Results and discussion

Three proprietary pouch cell LIBs were investigated under two trigger mechanisms for failure: thermal by external heating and mechanical by nail penetration. Temperature measurements taken of the thermally failed cell (Cell 2) and a video recorded during the nail penetration test on Cell 3 reveal the behaviours of each cell during failure. A subsequent post-mortem analysis investigated the responses of the cells in the context of architectural changes to the cell structure as a whole, the microstructure of the bulk electrode layers (anode and cathode) and the particle morphologies (cathode). Figure 3 (a) and (b) show photographs of the whole cell after both types of tests. Upon initial inspection, the outer casing of the thermally failed cell (Cell 2) was significantly charred and the cell was swollen with no visible ruptures. The nail penetrated cell (Cell 3) had a rupture through the cell as a result of the 100 % depth of penetration. The separator remained intact for Cell 3 suggesting that it did not reach temperatures above 120  $^{\circ}\text{C}$ , while the separator in the thermally failed cell had melted when temperatures reached > 120  $^{\circ}\text{C}$ . On disassembly of the cell, the Cu current collector of the anode in the nail penetrated cell appeared brittle and the tab



had detached from the bulk electrode layer stack. A comprehensive discussion of a post-mortem analysis using X-ray CT and SEM techniques follows, and is categorised according to the type of analysis: whole-cell and component.

### 3.1 Whole cell investigation

The whole cell analyses were carried out using the 'non-invasive' sample preparation technique. The cells pre- and post-failure were examined at two spatial resolutions as shown in Figure 4. The first set, using the Nikon X-ray macro-CT instrument achieved voxel sizes of 31.7  $\mu\text{m}$ , 33.6  $\mu\text{m}$ , and 27.8  $\mu\text{m}$  for the pristine cell (Cell 1), thermally failed (Cell 2) and the nail penetrated (Cell 3), respectively. The second set, using the Zeiss Xradia Versa X-ray micro-CT instrument with a 4 X objective lens (ROI scan with ca. 3 – 4 mm field of view), achieved voxel sizes of 1.83  $\mu\text{m}$ , 2  $\mu\text{m}$ , and 1.7  $\mu\text{m}$  for Cell 1 – 3, respectively. For the larger voxel size scans, the architecture of the whole cell, i.e. the outer casing of the pouch, the tabs, and the electrode layers (anode and cathode) are distinguishable based on their grayscale values. As a result, the behaviour of these features when subjected to different trigger mechanisms can be compared. For example, the outer casing and disorder in electrode layers in Cell 2 reveal that there was a greater pressure build-up and distribution within the thermally failed cell compared to that of the nail penetrated cell (Cell 3). The microstructure of the electrode layers also reveals where cracks formed and how they differ between the two types of failure. For the nail penetrated cell, the largest and most prominent cracks are all distributed directly above or below the nail, whereas cracks in the thermally failed cell are distributed across the whole cell architecture, but are concentrated in areas where kinks have occurred in the electrode layers due to large gas pockets. A more comprehensive analysis of the two failure types and comparisons with the pristine cell is reported in the following sections.

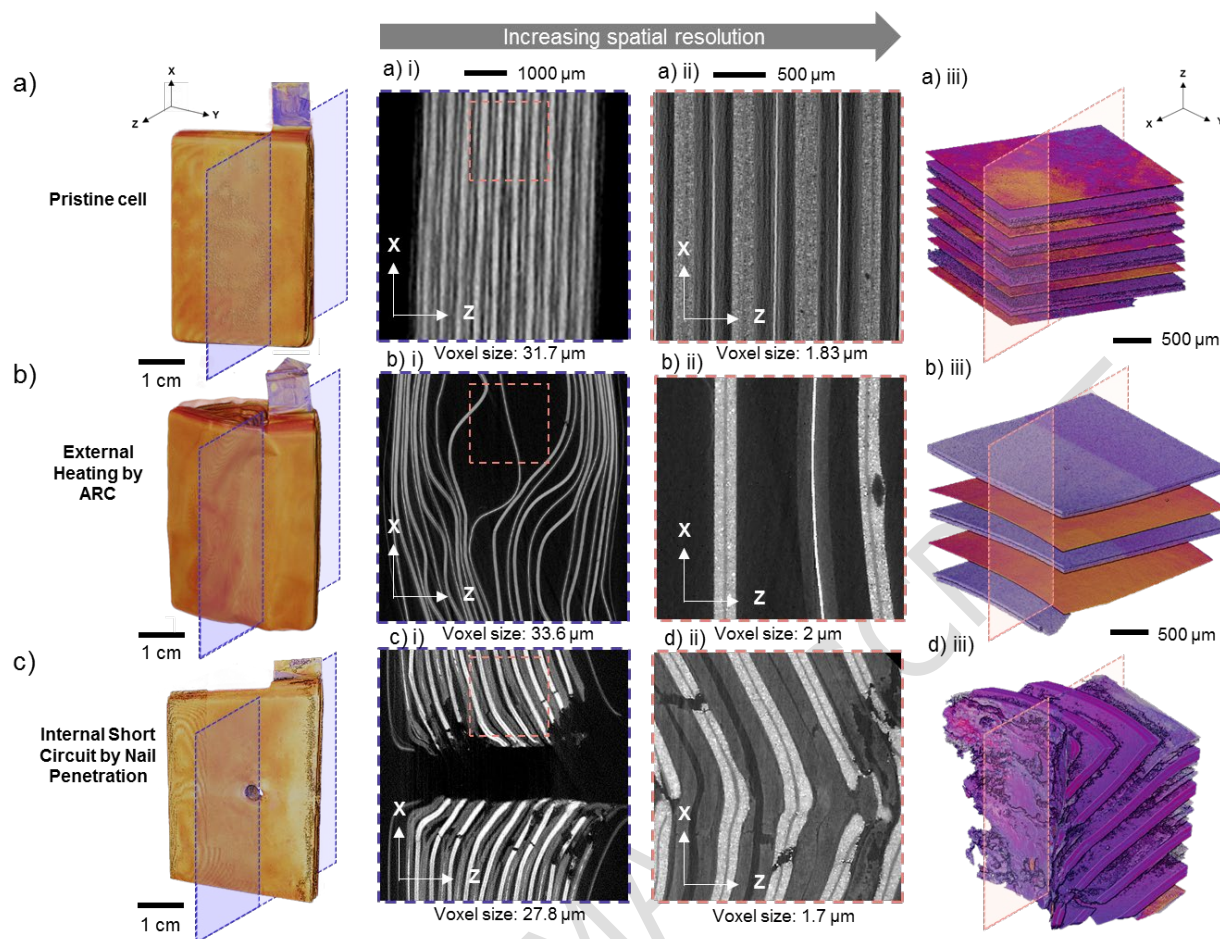


Figure 4 (a-c) show volume renderings and orthogonal slices in the XZ planes for the pristine cell (Cell 1), the thermally failed cell (Cell 2), and the nail penetrated cell (Cell 3), respectively. Corresponding scan numbers are 1 – 6 in Table S2 in SI.

### 3.1.1 Thermal failure: external heating by ARC

Increased reactivity due to external heating in lithium-ion batteries is often a consequence of SEI decomposition and exposure of the anode to the electrolyte causing self-heating reactions. When this heat is not well dissipated, the temperature of the cell continues to rise due to sustained exothermic reactions (often denoted the ‘acceleration’ stage). Further reactions involving electrolyte oxidation at the cathode surface eventually cause the cell to enter the ‘thermal runaway’ stage. During this stage, several high rate electrode reactions will continue to generate heat, and the cell may eventually catch fire and rupture. A typical self-heating rate used to characterise thermal runaway (TR) of a lithium-ion cell is  $10\text{ }^{\circ}\text{C min}^{-1}$  or higher. TR temperatures can vary between  $130\text{ }^{\circ}\text{C}$  to  $200\text{ }^{\circ}\text{C}$  or greater and are highly dependent on cell size, format, and materials. From Figure 5 (a), it appears that Cell 2 did not reach TR (i.e. a self-heating rate  $> 10\text{ }^{\circ}\text{C min}^{-1}$ ), however, visual inspection suggests significant

thermal damage by fire (charring of outer case). The temperature profile in Figure 5 (a) reveals that the self-heating rate between 60 °C and 130 °C remains below 1 °C min<sup>-1</sup>. The decomposition of SEI is typically expected to begin at 60 °C, exposing the anode surface to the reactive electrolyte. Exothermic reactions between the two are expected to occur at ca. 100 °C. Heat generation from this promotes an elevation of the cell temperature. The inflection at ca. 125 °C may be a result of the separator melting since the self-heating rate shortly after this reaches the > 1 °C min<sup>-1</sup> region. Shortly after the separator melts, short circuits between the Al and Cu current collectors may have caused a high local rate of Ohmic heat generation, as shown by the continuing rise in temperature in Figures 5 (a) and (b). After this point, decomposition of the anode is expected to continue and as the temperature nears 200 °C, the decomposition of the electrolyte, binders and cathode materials may also occur. However, in this test, the self-heating rate drops below 1 °C min<sup>-1</sup> at ca. 175 °C, this is suspected to be a result of the thermocouple detaching from the cell.

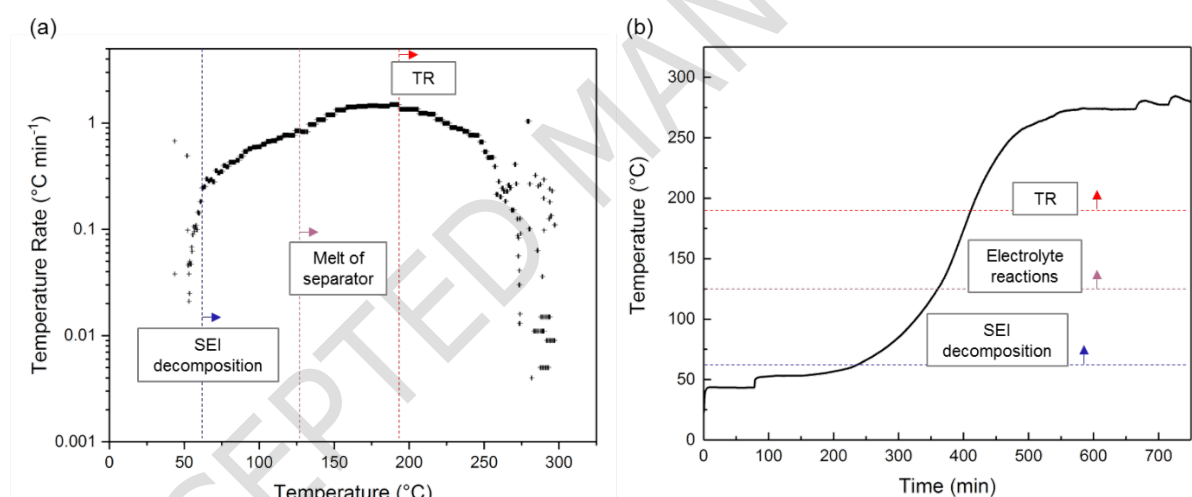


Figure 5 ARC self-heating rate profiles of a 1 Ah layered pouch cell. A start temperature of 50 °C was increased step-wise by 5 °C. (a) The inflection at ca. 125 °C shows the start of an increase in heat generation above 1 °C min<sup>-1</sup> (b) this can be seen in the curve before the plateau in the self-heating profile. At this temperature, it can be assumed that this attributes to the breakdown of the SEI layer.

While the temperature profiles begin to provide a dynamic, thermo-mechanical understanding of the phenomena occurring within the pouch cell during thermal failure, there is limited understanding of the mechanical dynamics: such as how heat and gas generated from the SEI decomposition dissipate through the cell or areas where short circuits may have occurred. Figure 6 (b) shows a 3D image of the whole cell after

thermal failure. The swelling of the outer pouch can be seen along with the dislocated electrode layers. The orthoslice views in the XZ and ZY planes offer an insight into the build-up of gas and the distribution of pressure within the cell. Orthoslice (position A) in the XZ plane (Figure 6 (a)) shows two distinct gaps where generated gas may have escaped through the vacuum seal vertically along the length of the cell. Orthoslice (position C) in the XZ plane reveals that there is a significantly larger space between the central (or 10<sup>th</sup>) layers vertically along the length of the cell; however this is not the case in the perpendicular direction which has an uneven displacement across all the layers as shown in Figure 6 (c) in orthoslice (position G). It is evident that venting of the cell also occurs across the seals close to the tabs from orthoslice (position E) in the ZY plane, as expected since this is mechanically the weakest point of the cell architecture. As there were no internal temperature measurements taken, it is difficult to predict the temperature distribution across the cell. However, a comparable pouch cell that underwent thermal runaway in literature suggests that the temperature distribution within a cell of this format is characteristically uneven and can result in a longer failure duration and more gradual mechanical expansion(51) when compared to a cylindrical cell for example(52). The distribution of melted materials (e.g. Al or Cu) within a cell during failure often indicates internal cell temperatures; for example, Finegan et al. report that molten Al remnants enhanced the heat dissipation of local exothermic reactions. For Cell 2, however, there are no visible globules of Al in the obtained X-ray CT images, suggesting the internal cell temperatures did not exceed the melting point of Al (> 660 °C).

The 2D orthoslice at a higher spatial resolution in Figure 6 (d), although limited by the field of view (3 mm), reveals the undisturbed electrode layer architecture in greater detail. In the two cathode and two anode layers visible, there does not seem to be significant delamination of the active cathode or anode layer from their respective current collectors (aluminium and copper). Although the image is taken at the centre of the cell, it is difficult to deduce with confidence which layer number it is in reference to the whole stack (20 layers). The defect highlighted in the cathode active layer is suspected to be due to a small defect from the cathode fabrication rather than as a result of the thermal failure. As expected, the separator layer is not visible as it had melted.

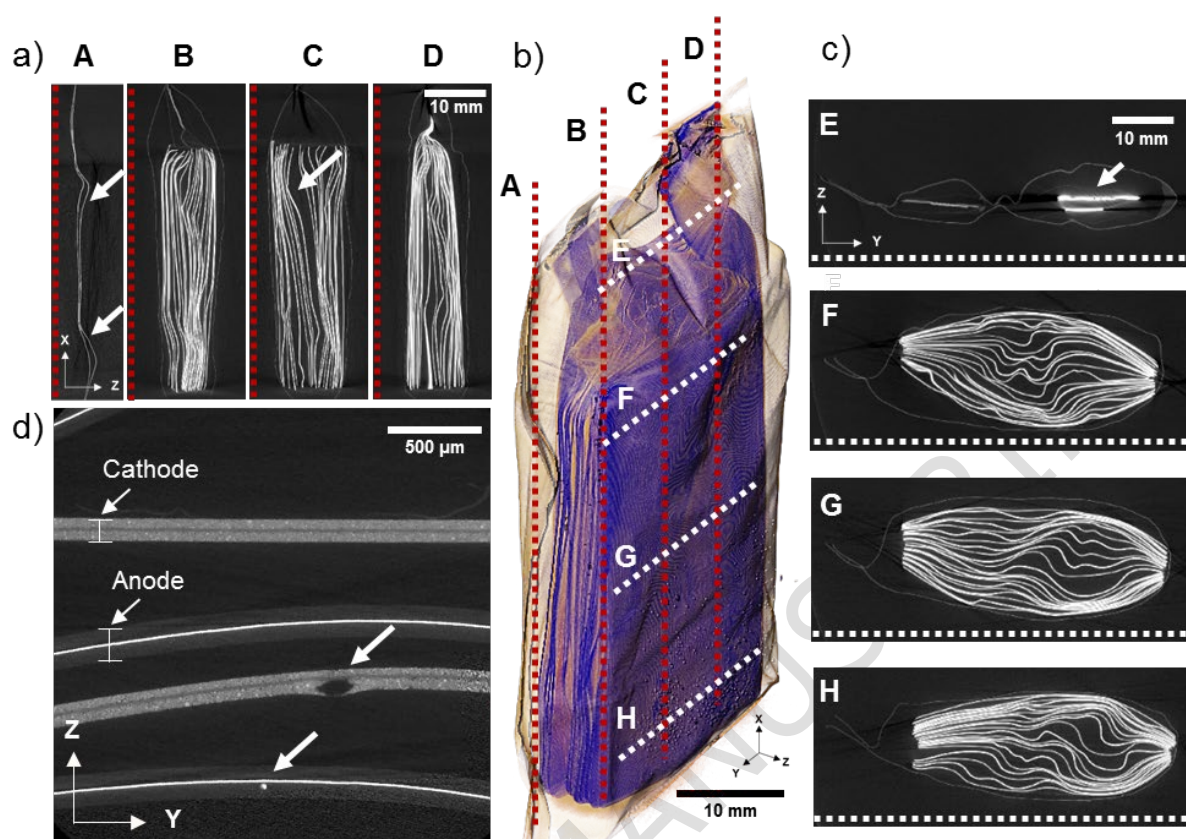


Figure 6 Images of pouch cell after thermal failure (Cell 2). Images from the whole cell X-ray CT scan in orthoslices along the (a) XZ planes and (c) ZY planes show the electrode architecture after deformation due to gas generation. The swelling of the outer casing is visible in (c) in the E, F, G and H positions (voxel size:  $33.6 \mu\text{m}$ ). The welded anode tab appears to be detached in (c) position E (where the bright white areas are the Cu current collector and Ni tab). A volume rendering in (b) shows the electrode layer architecture within the swollen outer casing, and (d) the orthoslice in the ZY plane with a voxel size of  $2 \mu\text{m}$ , shows defects in the cathode and anode layers. Corresponding scan numbers are 2 and 5 in Table S2 in SI.

### 3.1.2 Nail penetration: internal short circuit failure

Nail penetration can severely damage the internal components of the LIB. Metallic current collectors and separators with insufficient flexibility can fracture and cause direct contact between electrodes. As a result, heat is often generated after a localised short circuit and if the rate of heat dissipation is less than the rate of generation, thermal runaway may be initiated. The centre of Cell 3 was pierced by a nail during the test (100 % nail depth). It is believed that a large amount of heat may have generated local to the nail tip and the electrolyte may have decomposed shortly after the short circuit: firstly, from the heat generated, and secondly, from reacting with the oxygen entering through the rupture. The gas generation is predicted to have only lasted a short amount of time, and no thermal runaway occurred. The cell did not catch fire as recorded in the video (Cell 3\_Nail Penetration.mp4), and the photograph of the cell outer casing in Figure 3 (b) shows how the cell casing appears intact, aside from the point of nail ingress.

Figure 7 (b) shows X-ray CT images of the 1 Ah pouch cell after nail penetration and Figure 7 (a) shows the pristine, un-failed cell for comparison. From the orthoslice in the XZ plane of the whole cell scan in Figure 7 (b)(i), it is evident that all layers were affected by the nail penetration event as a result of the distribution of gas generation across the cell. A closer inspection in Figure 7 (b)(iv) reveals delamination of the cathode active material from the Al current collector across the whole cell, and at a greater degree concentrated near the point of nail ingress (positions A – E). The high specific heat and thermal conductivity of Al may have enhanced the dissipation of the heat generated from the electrolyte reactions. Fractures and cracks are also visible in the microstructure of the bulk electrode layers. When compared with the thermally failed cell (Cell 2), the estimated pressure (or disruption of electrode layers) within the nail penetrated cell is significantly smaller.

A combination of multiple failure behaviours is visible in the ROI scans with voxel size 1.7  $\mu\text{m}$  (Figure 7 (b)): the shear stress crossing multiple layers, fracture and breaking of current collectors and dislodging of electrode particles. Under tension, the electrodes' mechanical response is dominated by the property of the current collector(53). Furthermore, weak points caused by the intrusion of the active particles into the metal foil as a result of calendaring lower the tensile failure strain of the current collector(42). In the orthoslice in the XZ plane in Figure 7 (b), and XY plane in Figure



7 (b)(ii), (i.e. looking through the rupture in the direction of the nail), delamination of the anode material (graphite) from the Cu current collector is visible. The Cu current collector also appears to have disintegrated near the rupture. In some areas, the heated Cu likely reacted with oxygen from the surrounding air entering the cell and produced CuO (as can be seen in the green areas highlighted in the photographs of the cell after failure in Figure S3). The greyscale value of a material is dependent on its X-ray absorption coefficient. Highly attenuating materials are brighter and/or whiter, such as Cu, and those with lower attenuation coefficients, such as Al, are darker. There is little contrast between the greyscale values of Cu and CuO owing to their similar densities (8.96 and 6.0 g cm<sup>-3</sup>); as a result, it is difficult to distinguish this from the orthoslices in Figure 7 (b). Furthermore, Cu or CuO is only visible in small portions of the rupture.

The heat response of a nail penetration-induced short circuit event was not measured in this work, however, it is assumed that the temperature of the whole cell did not increase above 120 °C, the melting point of the polyethylene separator, as it was still intact after cell-opening.

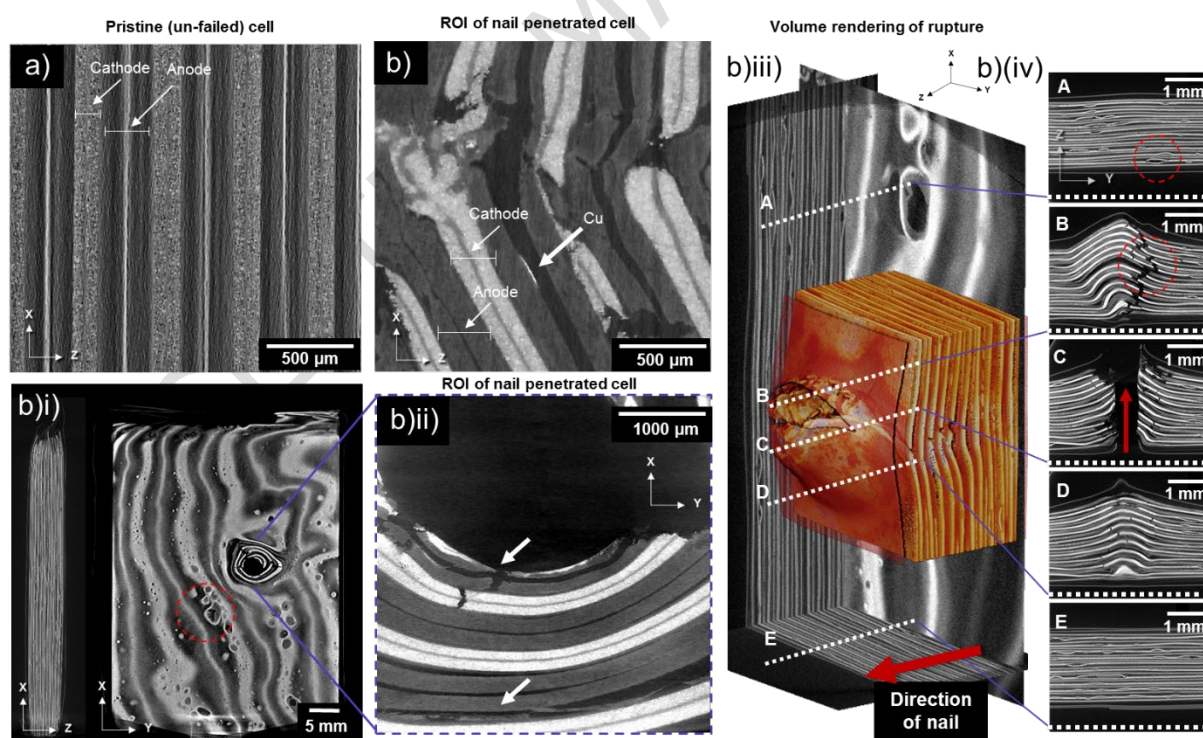


Figure 7 Orthoslice of the (a) pristine cell (Cell 1) in the XZ plane (voxel size: 1.83  $\mu\text{m}$ ) and orthoslice of the (b) nail penetrated cell (Cell 3) in various planes. The direction of the nail is highlighted in (b)(iii) where a volume rendering of the rupture is shown. Corresponding scan numbers are 3, 4, and, 6 in Table S2 in SI.

A volume rendering of the rupture and its corresponding orthoslices (in positions A – E) in Figure 7 (b)(iii) and (iv), respectively, show where breaks occurred. The rupture developed in both the transverse and nail direction, resembling the shape of a cross, as predicted by Sahraei et al. (42). Directly above the nail (in position B), a transverse fracture, vertically along the length of the cell, and the across all the layers is visible. Areas, where the current collectors have folded, can also be seen (i.e. where multiple short circuits may have occurred). It is not well known how the evolving microstructural fractures, cracks and folds influence the heat distribution leading up to and/or during the thermal runaway process.

Electrode particles near the rupture centre are severely dislodged which may also have contributed to the short circuit failure. However, it is difficult to confidently conclude whether this was a result of the nail entering (during failure) or leaving the cell (after failure).

## 3.2 Cell opening: component investigation

### 3.2.1 Bulk electrode layer

After opening the cells, the cathode, anode and separator were carefully separated (Figure 3). From the samples harvested from the thermally failed cell, both the anode and cathode displayed a non-homogeneous surface with some distinct deterioration as seen in Figure 3 (a)(ii-iii). Large, dark areas appear on the cathode surface primarily where the surface was still in contact with the anode surface. At temperatures greater than 120 °C, the SEI, binder materials and separator are expected to have melted(27). This is likely to be the reason why the cathode active layer was easily detached from the aluminium current collector during handling. The anode material in Figure 3 (a)(ii), in some regions, is detached from the copper current collector. Some darker areas on the surface are primarily due to the detachment of the material from the cathode following its degradation under high temperatures. For the samples taken from the nail penetrated cell (Figure 3 (b)(ii-iii)), there are some stark differences in the macroscopic appearance of the electrode surfaces: both surfaces have traces of the separator which melted in some areas. The cathode surface has some distinct features: the surface is rough, and areas where gas pockets formed causing the active material from the Al current collector to delaminate are visible.



Furthermore, the surface appears homogeneous in colour, compared to the thermally failed cathode, and it was easier to handle (no flaking). The anode layer in comparison displayed a non-homogeneous surface with some silver-grey areas possibly indicating lithium plating. In the areas close to the rupture (or hole left from the nail penetration), sections, where the Cu has oxidised, are visible in green. Darker regions are areas which are expected to be a result of some of the graphite layer being attached to the separator.

Figure 8 shows the SEM images of the pristine (a)(i – ii), thermally failed (b)(i) and, nail penetrated (c)(i) cathode materials as well as the thermally failed (b)(ii) and nail penetrated (c)(ii) anode materials. The cathode material of the pristine cell (Figure 8 (a)(i)) displays a uniform morphology with some dispersed binder, cracks and secondary particles. As seen in Figure 8 (a)(ii), the secondary particle is a spherical agglomerate constructed from primary particles. For the thermally failed cell, some microscopic features display areas where fragments from the melted separator and products from the electrolyte decomposition (i.e.  $\text{LiPF}_6$ ,  $\text{LiF}$ ,  $\text{PF}_5$ ) have accumulated(24). In comparison to the pristine cathode, there are fewer cracked particles. It is expected that temperatures above  $175\text{ }^\circ\text{C}$  would have resulted in the breakdown of the active cathode material(28), and the propagation of degradation may have occurred more due to the larger surface area than through particles with no visible micro-cracks(54). The microscopic appearance of the cathode surface after nail penetration in Figure 8 (c)(i) on the other hand appears unchanged when compared to the pristine cathode. This is further explored (for the nail penetrated cell) in Figure S8, where SEM images were taken from the top, middle and bottom samples of the central cathode layer to investigate the representativeness of the observed surface morphology. The appearance of the surface remains mostly uniform regardless of location, though the middle image (closest to the nail and rupture) appears to have a greater number of inter-particle voids, likely a result of gas expansion.

Figures 8 (b)(ii) and (c)(ii) show the morphology of the anode materials after thermal failure and nail penetration, respectively. After the breakdown of the SEI layer on the anode surface the exposed intercalated lithium reacts with the electrolyte solution. A thick deposited layer morphology and cracking of the layer is visible for the thermally failed anode; a single anode particle boundary cannot be distinguished through the layer which is predicted to be caused as a result of the decomposition

reactions occurring at temperatures above 150 °C(55). While images of the pristine anode were not collected in this work, comparisons with a pristine graphite anode surface in literature(20)(45) demonstrate how the surface of the anode after nail penetration remains relatively intact with regards to the appearance of clear boundaries. However, the particle surface displays some evidence of degradation/exfoliation which could be explained by the breakdown of the SEI at high temperatures causing new graphitic edges and plane fragments to be exposed at the surface.

Overall, the SEM images reveal important microscopic and surface level changes to the bulk electrode layers. While collecting the images is a relatively fast method and can cover a large area across the electrode surface, there are still several features, specifically delamination of the cathode and anode layers from their respective current collectors and microstructural parameters such as particle size distribution that are difficult to quantify from 2D images alone. The following section reports the findings from a 3D analysis of the bulk electrode layers using X-ray micro-CT.

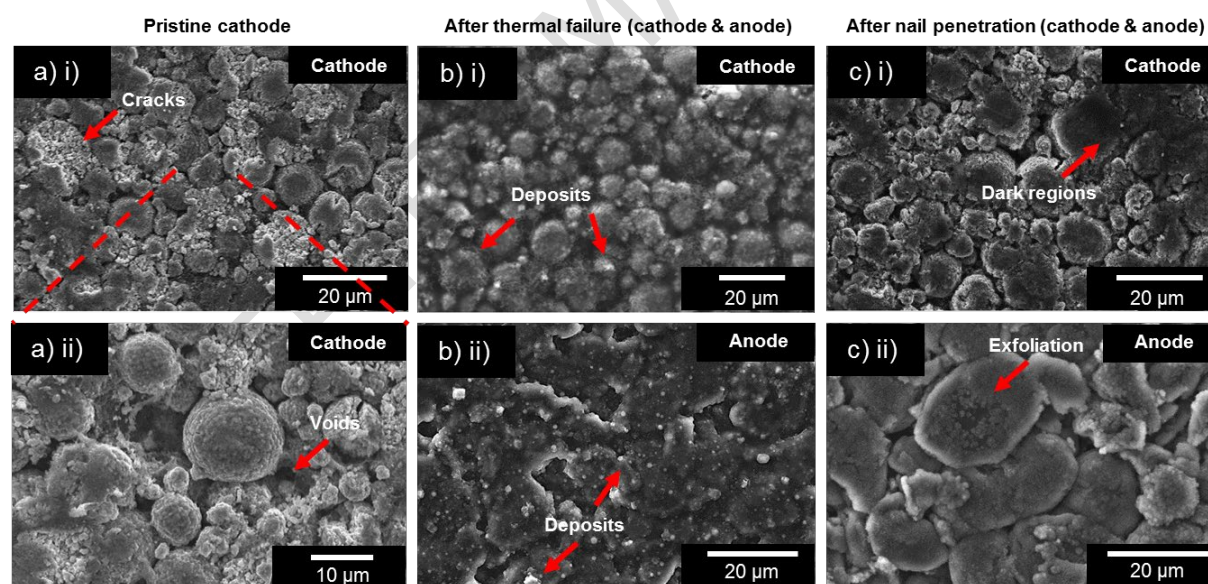


Figure 8 SEM micrographs of the (a)(i) pristine cathode at 3050 magnification (ii) and 4720 magnification, and the (b)(i) cathode, and (b)(ii) anode after thermal failure at approx. 3000 magnification. Similarly, the (c)(i) cathode, and (c)(ii) anode after nail penetration at approx. 3500 magnification.

The thermally failed and nail penetrated cells, Cells 2 and 3 respectively, were opened and samples of the anode and cathode electrode layers (0.4 mm x 0.4 mm

square) were extracted. Figure 9 shows orthoslices in the XY and XZ planes and their corresponding volume renderings from X-ray micro-CT scans. A visual comparison between the two cathodes (thermally failed and nail penetrated) reveals that there is no significant change to the bulk electrode structure. Further comparison with the pristine cathode bulk layer in Figure S4 confirms there is little difference (at this resolution) from the fresh state to the failed. Anode samples from both cells follow the same trend.

The particle size distribution (PSD) of the pristine cathode sample is compared to that of the post-mortem samples: thermally failed (Cell 2) and nail penetrated (Cell 3). Table S2 summarises the PSD findings, as well as the particle volume fraction, tortuosity factor and surface area per volume extracted from the datasets. The mean diameter extracted from the pristine bulk cathode layer is 5.39  $\mu\text{m}$ , and the mean diameters for the samples extracted from Cells 2 and 3 were 4.76  $\mu\text{m}$  and 6.10  $\mu\text{m}$ , respectively. It is difficult to confidently conclude a trend from the mean particle diameters extracted from the bulk electrode layers due to the limited resolution of the X-ray technique and the small sample size. However, the spread of data in the PSD (Figure S5 (a-c)) shows there is an additional peak below 2.5  $\mu\text{m}$  for both the failed cathode layers when compared to the pristine cathode. This is predicted to be a result of debris, fractured surface particles and/or delamination of particles from the Al current collector. Figure 11 shows the percentage change of parameters extracted from the bulk cathode layers of Cell 2 (thermal failure) and Cell 3 (nail penetration) from the pristine bulk cathode layer.

There are a greater number of particles with a diameter < 1  $\mu\text{m}$  in the thermally failed cathode layer compared with the nail penetrated sample. This is not reflected in the particle volume fractions and the surface area per volume for the three samples (Table S2), which are, in the same order, 0.46, 0.40 and 0.48, and 0.478, 0.408, 0.490. The particles that underwent thermal failure (and reached temperatures > 250  $^{\circ}\text{C}$ ) exhibit the lowest surface area per volume, which contradicts what is expected: the smaller the particle size, the lower the thermal stability of the material(56). The temperature profile of the nail penetrated cell (Cell 3) was not measured, however, from literature(41)(39), it is predicted that the temperature of the nail tip for this cell type may have exceeded 120  $^{\circ}\text{C}$  and initiated localised heat generation: causing the electrolyte to boil and generate gas(27).

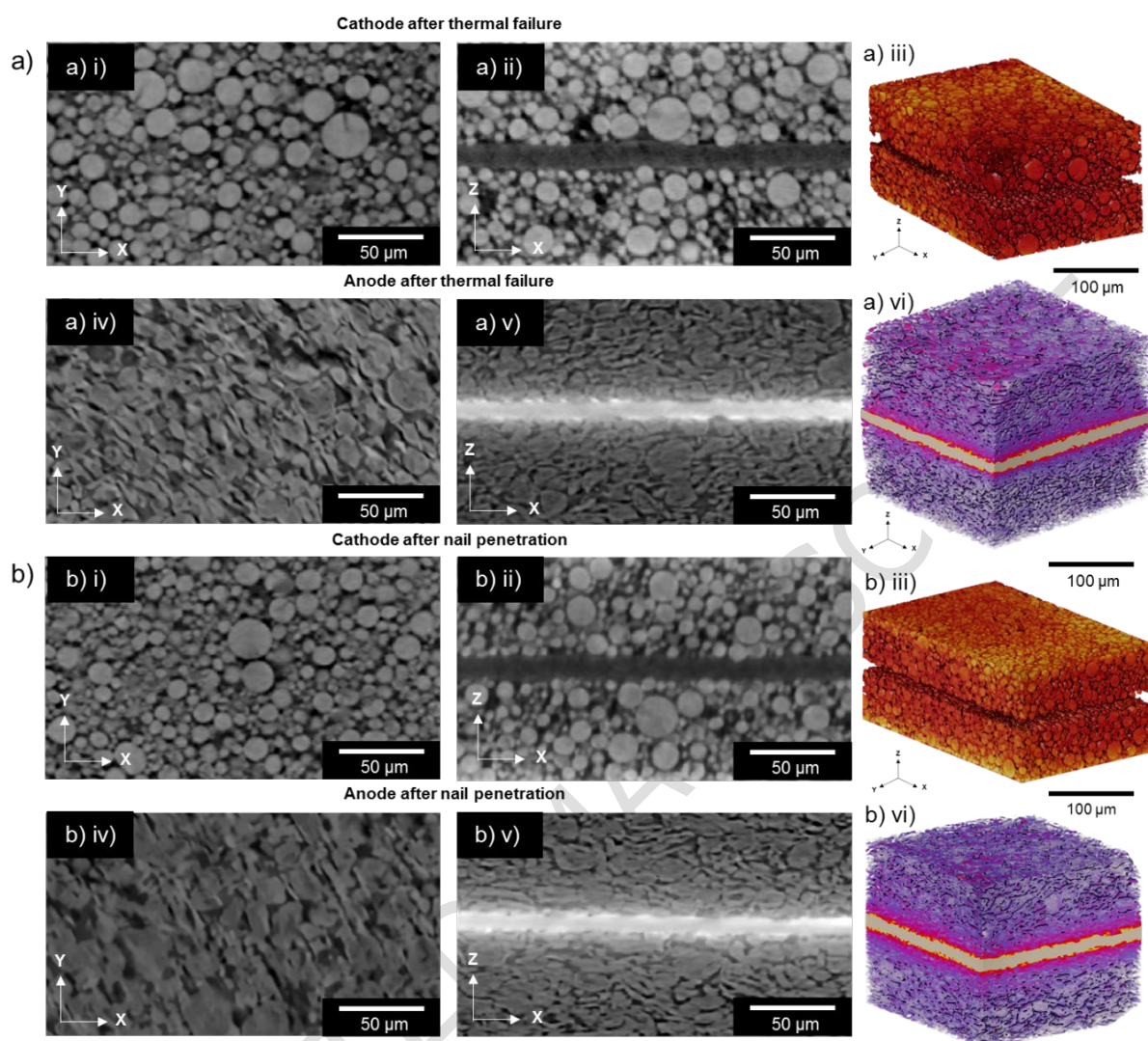


Figure 9 Orthoslices in the XY and XZ planes, and volume renderings, of the (a)(i – iii) cathode and (a)(iv – vi) anode after thermal failure and (b)(i – iii) cathode and (b)(iv – vi) anode after nail penetration. Corresponding scan numbers are 8 – 11 in Table S2 in SI.

The bulk anode layer from Cell 2 has a greater mean particle diameter, 16.99 μm than the sample from Cell 3, 13.59 μm. However, the pore volume fraction (0.31 and 0.36), surface area per volume (0.654 and 0.660), and tortuosity factor (2.97 and 3.19), of the thermally failed and nail penetrated anodes are similar. The surfaces of the two anodes in Figures 8 (b)(ii) and (c)(ii) show the structure of the effects of heating to temperatures > 250 °C and the extent of decomposition and deposits on the surface of the thermally failed anode. However, the 3D analysis shows how the anode and its microstructural properties remained intact below the surface. This is reflected in the spread of data of the PSD (Figure S6 (a – b)) where there are a greater number of

particles with diameters  $> 25 \mu\text{m}$  for the thermally failed anode, which is expected to be those furthest away from the current collector and shown in the 2D surface images.

From the whole cell scans, there were obvious areas where the cathode and anode layers had delaminated from their respective current collectors. However, due to the small sample size ( $0.4 \text{ mm} \times 0.4 \text{ mm}$ ) required for the bulk electrode layer scans, it is difficult to directly observe this phenomenon. Furthermore, despite using the whole cell scans to predict where to extract samples; it was still difficult to pinpoint an area where delamination had occurred. Bulk electrode layer scans are useful for determining key material characteristics such as particle size distributions and tortuosity. They are especially useful for understanding heat distribution across layers within a whole cell, however, they are limited by their sample size and may not give a full representation of the phenomena that occurred during failure.

### 3.2.2 Electrode particles

Figure 10 (a)(i) shows the cathode in its pristine state at a voxel resolution of  $0.0631 \mu\text{m}$ , in the XZ plane. Similarly, Figures 10 (b)(i) and (c)(i) show the cathode extracted from the thermally failed and nail penetrated cells, at voxel resolutions of  $0.126 \mu\text{m}$ . All three samples clearly show two phases: particle (light grey) and pore/carbon binder domain (dark grey). It is difficult to distinguish between the pore and CBD at this resolution(57). The mean particle diameters are  $2.93 \mu\text{m}$  (pristine),  $4.43 \mu\text{m}$  (thermally failed) and  $4.47 \mu\text{m}$  (nail penetrated). When compared to the Versa datasets, the pristine cathode has an unexpectedly small mean particle diameter in comparison to that extracted from the pristine bulk cathode layer ( $5.39 \mu\text{m}$ ). This may have a direct correlation to the number of intra-particle cracks within the pristine sample. For example, the label analysis carried out during the PSD extraction may have assigned a single particle that was cracked in two as two separate particles with smaller diameters. As a result, the greater the number of particle cracks; the greater the number of smaller particle sizes in the PSD(58). Figure 11 highlights the extent of variation of the parameters extracted from the bulk electrode layer (micro-) and particle morphology (nano-CT) 3D images. The surface area per volume of the post-failure cathode particles showed the greatest increase when compared to the surface area per volume of the pristine particles. This could be attributed to the changes in the



particle morphology and/or orientation within the cathode layer as a result of the failure mechanisms(59)(60). Nevertheless, it is still important to consider the sample volume and its statistical significance here, while this resolution helps elucidate certain particle features, it is difficult to confidently compare the PSD trends obtained from the bulk electrode layers that have greater sample sizes/bounding box dimensions (see Table S2). A representative volume analysis of the particle scans shown in Figure S7 however illustrates the accuracy of the pore volume fraction and tortuosity factors across the sample sizes for Ultra scans ( $< 65 \mu\text{m}$ ).

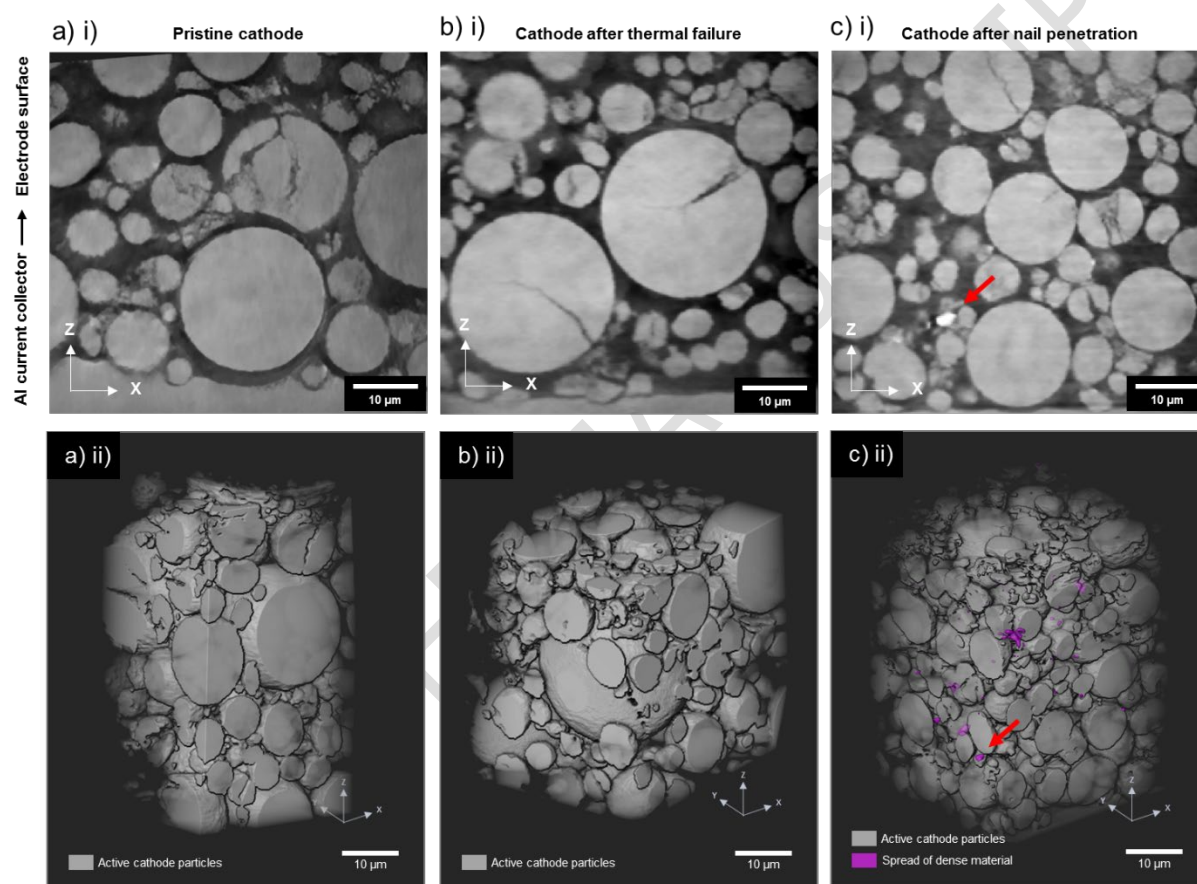


Figure 10 Orthoslices in the XZ plane of the cathode acquired using X-ray nano-CT for (a)(i) the pristine, (b)(i) after thermal failure (Cell 2), and (c)(i) after nail penetration (Cell 3) samples. The Al current collector is at the bottom (visible in (a)(i) and (b)(i)) and the electrode surface is at the top. A highly attenuating spot is highlighted in (c)(i). Volume renderings of the (a – c)(ii) pristine, Cell 2, and Cell 3, show the particles after segmentation. The denser material deposits are highlighted by the red arrow. Corresponding scan numbers are 12 – 14 in Table S2 in SI.

The particles within the cathode layer after nail penetration display some bright regions, highlighted in the greyscale image in Figure 10 (c)(i). The brighter regions represent a highly attenuating/dense material, such as Co or Cu due to their high

atomic masses. Figure 7 (b) displayed dislodging of electrode particles, however, it is difficult to predict the precise cause of the contamination in ex-situ. Typically, when a cell is forced to over-discharge, the cell voltage drops below the safe cut-off voltage. The nail penetration event is expected to have caused a localised internal short circuit and triggered similar mechanisms to that of an over-discharge(61): rapid delithiation of the anode and lithiation of the cathode. As the anode potential increases it can overcome the overpotential required for Cu dissolution, as a result, Cu is oxidised.  $\text{Cu}^+/\text{Cu}^{2+}$  ions may penetrate the separator and become deposited on the cathode surface. A volume rendering in Figure 10 (c)(ii) shows the spread of the dense material within the cathode layer (acquired using X-ray nano-CT). The volume fraction of the dense material is 0.00028, making it difficult to distinguish in the SEM (Figure 8 (c)(i)) or micro-CT (Figure 9 (b)) images.

There are several micro-cracks, which don't span the entire particle diameter, and shattered particles, which present as small fragments across all three cathode samples (pristine, thermally failed and nail penetrated). It is predicted that the presence of these cracks is more likely to be a result of the manufacturing process (via calendaring)(54) than as a result of thermal and/or short circuit failure. Furthermore, Figure 10 (a – b)(i) shows areas where the active particles have intruded into the aluminium foil as a result of calendaring, suggesting that the local stress concentrations(62) were high enough to deform the current collector sheet, and subsequently high enough to induce micro-cracks and particle shattering.

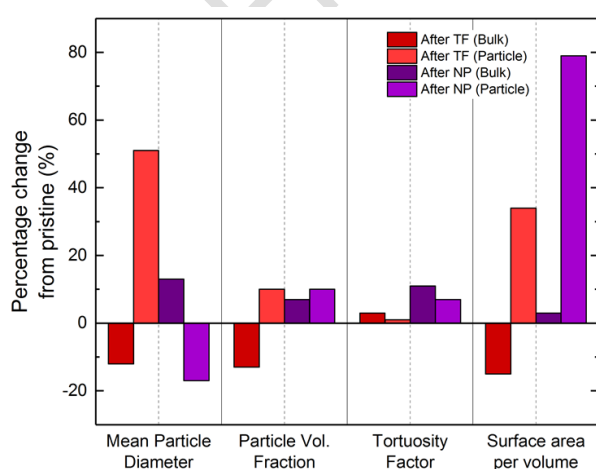


Figure 11 (a) Percentage change for the mean particle diameter, particle volume fraction, tortuosity factor and, surface area per volume, of the micro-CT bulk electrode layer image (Bulk), and nano-CT

*image (Particle) of the thermally failed (TF) and nail penetrated (NP) cathode layers, from the pristine cathode layer and particle scans. A positive percentage represents an increase, and a negative represents a decrease. Corresponding scan numbers are 7, 9, 11 – 14 in Table S2 in SI.*

## 4 Conclusion

Although LIBs are a suitable choice for the future of energy storage, concerns regarding their safety impede their widespread use in some sectors. LIBs can fail by multiple different failure mechanisms across their multi-layered structures and scales. While they're extensively investigated and tested at a whole and particle scale, there is limited standardisation across the methodologies for safety testing and post-mortem analyses. In this work, we present an outline for the use of X-ray CT to investigate failure mechanisms by invasive and non-invasive methods.

At present, whole-cell X-ray CT is used to investigate the architecture of a battery post-failure concerning its electrode deformation and/or safety features. Oftentimes it is used as a technique to determine specific areas of interest, for example, dendrite growth, electrode folds, tab placement etc. This work showcased the benefits of ROI scans at voxel resolutions between 1.7 - 2  $\mu\text{m}$  in post-mortem cells. The whole cell X-ray CT in this work offered a method to investigate the volume change due to swelling, gas dispersion and bulk electrode behaviour from various stresses (heat and gas generation and puncture with a nail) within the cells without disturbing their delicate environments.

While invasive measurements yielded useful bulk electrode layer and particle parameters, they did not demonstrate a full representation of the failure phenomena. The post-mortem analysis by SEM is a relatively faster analysis method, however conclusions made solely from 2D images gave only a surface level understanding and key features such as particle mixing and/or electrode delamination were difficult to identify. X-ray micro- and nano-CT of the bulk electrode layer and particle morphologies were more useful for understanding the particle behaviour as a whole, e.g. PSDs and cracking and how they may have affected heat dissipation throughout the cell, however, they were also proven to be insufficiently representative and were limited by the size of the sample. Furthermore, the overall technique requires complex sample preparation techniques which can make it a relatively slow method for



commercial post-mortem analyses. Of the two failure mechanisms, the thermally failed cell appeared to undergo a more severe failure. It reached a higher maximum temperature and had significantly more damage across various length scales from its whole cell architecture (swelling and distribution of gas), layers (melted separator) and electrode surfaces (deposits). The nail penetrated cell, on the other hand, was relatively less severe: the majority of its outer shell casing remained intact and heat dissipated through the cell more uniformly.

X-ray CT has proven to be a useful tool for LIB failure analysis. Its widespread deployment in commercial LIB failure testing and analysis has often been limited by accessibility in terms of the high cost of equipment and time taken per scan. However, this is quickly changing as new research efforts aim to take better advantage of their capabilities; for example by developing methods for optimal sample preparation and faster acquisition times. Furthermore, it is important to note that due to the limited number of repeat tests presented here, conclusions with high confidence cannot be drawn from these results. Nevertheless, these results demonstrate the use of non-invasive X-ray CT for evaluating the effects of thermal and internal short circuit failures on the materials within LIBs, and this work flow, now established, can be readily applied to parametric studies of battery failure.

### <Acknowledgements>

This work was supported by the Engineering and Physical Sciences Research Council, EPSRC (EP/N032888/1, EP/R020973/1, EP/K005030/1, EP/M028100/1). DP acknowledges funding from the EPSRC CASE Award scheme with Johnson Matthey. PRS acknowledges the support of The Royal Academy of Engineering (CiET1718/59) and The Faraday Institution (EP/S003053/1), grant number FIRG001.

## 5 References

1. G. E. Blomgren 2017, **164**, (1), 5019 LINK <https://doi.org/10.1149/2.0251701jes>
2. N. Nitta, F. Wu, J. T. Lee and G. Yushin, *Mater. Today*, 2015, **18**, (5), 252 LINK <https://doi.org/10.1016/j.mattod.2014.10.040>
3. D. H. Doughty and E. P. Roth, *Interface Mag.*, 2012, **21**, (2), 37 LINK <https://doi.org/10.1149/2.F03122if>
4. P. G. Balakrishnan, R. Ramesh and T. Prem Kumar, *J. Power Sources*, 2006, **155**, (2), 401 LINK <https://doi.org/10.1016/j.jpowsour.2005.12.002>
5. M. Jacoby, 'Assessing The Safety Of Lithium-Ion Batteries', Chemical and Engineering News 2013
6. L. Bravo Diaz, X. He, Z. Hu, F. Restuccia, M. Marinescu, J. V. Barreras, Y. Patel, G. Offer and G. Rein, *J. Electrochem. Soc.*, 2020, **167**, (9), 090559 LINK <https://doi.org/10.1149/1945-7111/aba8b9>
7. Reuters, 'Sony Recalls PC Batteries' 2008 : <https://www.reuters.com/article/us-sony-battery/sony-recalls-pc-batteries-idUSTRE49U1EZ20081031>
8. Reuters, 'Note 7 Fiasco Could Burn a \$17 Billion Hole Samsung Accounts' 2016 : <https://www.reuters.com/article/us-samsung-elec-smartphones-costs/note-7-fiasco-could-burn-a-17-billion-hole-in-samsung-accounts-idUSKCN12B0FX>
9. M. J. Loveridge, G. Remy, N. Kourra, R. Genieser, A. Barai, M. J. Lain, Y. Guo, M. Amor-Segan, M. A. Williams, T. Amietszajew, M. Ellis, R. Bhagat and D. Greenwood, *Batteries*, 2018, **4**, (1), 1 LINK <https://doi.org/10.3390/batteries4010003>
10. E. Musk, 'Model S Fire', Tesla Blog 2013 : [https://www.tesla.com/en\\_GB/blog/model-s-fire](https://www.tesla.com/en_GB/blog/model-s-fire)
11. Reuters, 'Tesla Top-of-Range Car Caught Fire While Owner Was Driving, Lawyer

- Says', Autos & Transportation 2021 : <https://www.reuters.com/business/autos-transportation/tesla-top-of-range-car-caught-fire-while-owner-was-driving-lawyer-says-2021-07-02/>
12. InsideEVs, 'Jaguar I-Pace Catches Fire While Charging In Hungary' 2021 : <https://insideevs.com/news/544255/jaguar-ipace-charging-fire-hungary/>
  13. UNECE Transport Division, 'Statistics and Analysis on Fire Accidents for EVs', in 'EVS 16th Sess.', Gothenburg, 2018 LINK <https://wiki.unece.org/display/trans/EVS+16th+session>
  14. Addionics, 'Pouch, Cylindrical or Prismatic: Which Battery Format Will Rule the Market?' 2021 : <https://www.addionics.com/post/pouch-cylindrical-or-prismatic-which-battery-format-will-rule-the-market>
  15. J. Lamb, C. J. Orendorff, L. A. M. Steele and S. W. Spangler, *J. Power Sources*, 2015, **283**, 517 LINK <https://doi.org/10.1016/j.jpowsour.2014.10.081>
  16. Y. Chen, Y. Kang, Y. Zhao, L. Wang, J. Liu, Y. Li, Z. Liang, X. He, X. Li, N. Tavajohi and B. Li, *J. Energy Chem.*, 2021, **59**, 83 LINK <https://doi.org/10.1016/j.jechem.2020.10.017>
  17. X. Feng, M. Ouyang, X. Liu, L. Lu, Y. Xia and X. He, *Energy Storage Mater.*, 2018, **10**, (December 2016), 246 LINK <https://doi.org/10.1016/j.ensm.2017.05.013>
  18. D. Doughty, 'Li Ion Battery Safety and Abuse Tolerance Report', Total Battery Consulting, Industry Report: Battery Safety 2019 : <https://totalbatteryconsulting.com/industry-reports/Battery-safety-report/overview.html>
  19. O. S. Mendoza-Hernandez, H. Ishikawa, Y. Nishikawa, Y. Maruyama and M. Umeda, *J. Power Sources*, 2015, **280**, 499 LINK <https://doi.org/10.1016/j.jpowsour.2015.01.143>
  20. B. Mao, H. Chen, Z. Cui, T. Wu and Q. Wang, *Int. J. Heat Mass Transf.*, 2018, **122**, 1103 LINK <https://doi.org/10.1016/j.ijheatmasstransfer.2018.02.036>
  21. V. Ruiz, A. Pfrang, A. Kriston, N. Omar, P. Van den Bossche and L. Boon-Brett, *Renew. Sustain. Energy Rev.*, 2018, **81**, (July 2017), 1427 LINK <https://doi.org/10.1016/j.rser.2017.05.195>



22. R. Spotnitz and J. Franklin, *J. Power Sources*, 2003, **113**, (1), 81 LINK  
[https://doi.org/10.1016/S0378-7753\(02\)00488-3](https://doi.org/10.1016/S0378-7753(02)00488-3)
23. H. Maleki, *J. Electrochem. Soc.*, 1999, **146**, (9), 3224 LINK  
<https://doi.org/10.1149/1.1392458>
24. E. P. Roth and D. H. Doughty, *J. Power Sources*, 2004, **128**, (2), 308 LINK  
<https://doi.org/10.1016/j.jpowsour.2003.09.068>
25. P. J. Bugryniec, J. N. Davidson, D. J. Cumming and S. F. Brown, *J. Power Sources*, 2019, **414**, (January), 557 LINK  
<https://doi.org/10.1016/j.jpowsour.2019.01.013>
26. W. C. Chen, Y. W. Wang and C. M. Shu, *J. Power Sources*, 2016, **318**, 200 LINK  
<https://doi.org/10.1016/j.jpowsour.2016.04.001>
27. X. Feng, M. Fang, X. He, M. Ouyang, L. Lu, H. Wang and M. Zhang, *J. Power Sources*, 2014, **255**, 294 LINK <https://doi.org/10.1016/j.jpowsour.2014.01.005>
28. Q. Wang, B. Mao, S. I. Stoliarov and J. Sun, *Prog. Energy Combust. Sci.*, 2019, **73**, 95 LINK <https://doi.org/10.1016/j.pecs.2019.03.002>
29. T. D. Hatchard, D. D. Macneil, A. Basu and J. R. Dahn, *J. Electrochem. Soc.*, 2001, **148**, (7), A755 LINK <https://doi.org/10.1149/1.1377592>
30. G. H. Kim, A. Pesaran and R. Spotnitz, *J. Power Sources*, 2007, **170**, (2), 476 LINK <https://doi.org/10.1016/j.jpowsour.2007.04.018>
31. D. Ren, X. Liu, X. Feng, L. Lu, M. Ouyang, J. Li and X. He, *Appl. Energy*, 2018, **228**, (July), 633 LINK <https://doi.org/10.1016/j.apenergy.2018.06.126>
32. C. F. Lopez, J. E. Soc, C. F. Lopez, J. A. Jeevarajan and P. P. Mukherjee 2015, LINK <https://doi.org/10.1149/2.0751510jes>
33. J. Zhu, T. Wierzbicki and W. Li, *J. Power Sources*, 2018, **378**, (November 2017), 153 LINK <https://doi.org/10.1016/j.jpowsour.2017.12.034>
34. T. Waldmann, A. Iturrondobeitia, M. Kasper, N. Ghanbari, E. Bekaert, L. Daniel, S. Genies, I. Jim, E. De Vito and M. Wohlfahrt-mehrens 2016, LINK <https://doi.org/10.1149/2.1211609jes>
35. C. J. Mikolajczak, T. Hayes, D. Ph, M. V Megerle, M. Wu and D. Ph 2007, 8




36. N. Williard, B. Sood, M. Osterman and M. Pecht 2011, 1616 LINK  
<https://doi.org/10.1007/s10854-011-0452-4>
37. D. P. Finegan, M. Scheel, J. B. Robinson, B. Tjaden, I. Hunt, T. J. Mason, J. Millichamp, M. Di Michiel, G. J. Offer, G. Hinds, D. J. L. Brett and P. R. Shearing, *Nat. Commun.*, 2015, **6**, 6924 LINK <https://doi.org/10.1038/ncomms7924>
38. D. P. Finegan, E. Darcy, M. Keyser, B. Tjaden, T. M. M. Heenan, R. Jervis, J. J. Bailey, R. Malik, N. T. Vo, O. V. Magdysyuk, R. Atwood, M. Drakopoulos, M. DiMichiel, A. Rack, G. Hinds, D. J. L. Brett and P. R. Shearing, *Energy Environ. Sci.*, 2017, **10**, (6), 1377 LINK <https://doi.org/10.1039/c7ee00385d>
39. D. P. Finegan, J. E. Soc, D. P. Finegan, B. Tjaden, T. M. M. Heenan, R. Jervis, M. Di Michiel, A. Rack, G. Hinds, D. J. L. Brett and P. R. Shearing 2017, LINK <https://doi.org/10.1149/2.1501713jes>
40. D. Patel, J. B. Robinson, S. Ball, D. J. L. Brett and P. R. Shearing, *J. Electrochem. Soc.*, 2020, **167**, (9), 090511 LINK <https://doi.org/10.1149/1945-7111/ab7fb6>
41. T. Yokoshima, D. Mukoyama, F. Maeda, T. Osaka, K. Takazawa, S. Egusa, S. Naoi, S. Ishikura and K. Yamamoto, *J. Power Sources*, 2018, **393**, (February), 67 LINK <https://doi.org/10.1016/j.jpowsour.2018.04.092>
42. E. Sahraei, M. Kahn, J. Meier and T. Wierzbicki, *RSC Adv.*, 2015, 80369 LINK <https://doi.org/10.1039/c5ra17865g>
43. R. F. Ziesche, T. Arlt, D. P. Finegan, T. M. M. Heenan, A. Tengattini, D. Baum, N. Kardjilov, H. Markötter, I. Manke, W. Kockelmann, D. J. L. Brett and P. R. Shearing, *Nat. Commun.*, (n.d.) (III), 1 LINK <https://doi.org/10.1038/s41467-019-13943-3>
44. N. Zhang and H. Tang, *J. Power Sources*, 2012, **218**, 52 LINK <https://doi.org/10.1016/j.jpowsour.2012.06.071>
45. W. Wu, R. Ma, J. Liu, M. Liu, W. Wang and Q. Wang, *Int. J. Heat Mass Transf.*, 2021, **170**, 121024 LINK <https://doi.org/10.1016/j.ijheatmasstransfer.2021.121024>
46. D. P. Finegan, M. Scheel, J. B. Robinson, B. Tjaden, M. Di Michiel, G. Hinds, D. J. L. Brett and P. R. Shearing, *Phys. Chem. Chem. Phys.*, 2016, **18**, (45), 30912 LINK <https://doi.org/10.1039/C6CP04251A>

47. X. Y. Yao and M. G. Pecht, *IEEE Access*, 2019, **7**, 24082 LINK <https://doi.org/10.1109/ACCESS.2019.2899793>
48. L. Salvo, M. Suéry, A. Marmottant, N. Limodin and D. Bernard, '3D Imaging in Material Science: Application of X-Ray Tomography', 'Comptes Rendus Phys.', 2010 LINK <https://doi.org/10.1016/j.crhy.2010.12.003>
49. S. J. Cooper, A. Bertei, P. R. Shearing, J. A. Kilner and N. P. Brandon, *SoftwareX*, 2016, **5**, 203 LINK <https://doi.org/10.1016/j.softx.2016.09.002>
50. J. J. Bailey, T. M. M. Heenan, D. P. Finegan, X. Lu, S. R. Daemi, F. Iacoviello, N. R. Backeberg, O. O. Taiwo, D. J. L. Brett, A. Atkinson and P. R. Shearing, *J. Microsc.*, 2017, **267**, (3), 384 LINK <https://doi.org/10.1111/jmi.12577>
51. M. T. M. Pham, J. J. Darst, D. P. Finegan, J. B. Robinson, T. M. M. Heenan, M. D. R. Kok, F. Iacoviello, R. Owen, W. Q. Walker, O. V. Magdysyuk, T. Connolley, E. Darcy, G. Hinds, D. J. L. Brett and P. R. Shearing, *J. Power Sources*, 2020, **470**, (June), 228039 LINK <https://doi.org/10.1016/j.jpowsour.2020.228039>
52. J. B. Robinson, J. A. Darr, D. S. Eastwood, G. Hinds, P. D. Lee, P. R. Shearing, O. O. Taiwo and D. J. L. Brett, *J. Power Sources*, 2014, **252**, 51 LINK <https://doi.org/10.1016/j.jpowsour.2013.11.059>
53. C. Zhang, J. Xu, L. Cao, Z. Wu and S. Santhanagopalan, *J. Power Sources*, 2017, **357**, 126 LINK <https://doi.org/10.1016/j.jpowsour.2017.04.103>
54. T. M. M. Heenan, A. Wade, C. Tan, J. E. Parker, D. Matras, A. S. Leach, J. B. Robinson, A. Llewellyn, A. Dimitrijevic, R. Jervis, P. D. Quinn, D. J. L. Brett and P. R. Shearing, *Adv. Energy Mater.*, 2020, **10**, (47), LINK <https://doi.org/10.1002/aenm.202002655>
55. D. P. Abraham, E. P. Roth, R. KostECKI, K. McCarthy, S. MacLaren and D. H. Doughty, *J. Power Sources*, 2006, **161**, (1), 648 LINK <https://doi.org/10.1016/j.jpowsour.2006.04.088>
56. J. Geder, H. E. Hoster, A. Jossen, J. Garche and D. Y. W. Yu, *J. Power Sources*, 2014, **257**, 286 LINK <https://doi.org/10.1016/j.jpowsour.2014.01.116>
57. S. R. Daemi, C. Tan, P. R. Shearing, S. J. Cooper, J. Cookson, T. Volkenandt, A. Palacios-Padros and D. J. L. Brett, *ACS Appl. Energy Mater.*, 2018, **1**, (8), 3702 LINK <https://doi.org/10.1021/acsaem.8b00501>

58. F. Rçder, S. Sonntag, D. Schrçder and U. Krewer 2016, 1588 LINK <https://doi.org/10.1002/ente.201600232>
59. O. O. Taiwo, D. P. Finegan, D. S. Eastwood, J. L. Fife, L. D. Brown, J. A. Darr, P. D. Lee, D. J. Brett and P. R. Shearing, *J. Microsc.*, 2016, **263**, (3), 280 LINK <https://doi.org/10.1111/jmi.12389>
60. X. Lu, A. Bertei, D. P. Finegan, C. Tan, S. R. Daemi, J. S. Weaving, K. B. O. Regan, T. M. M. Heenan, G. Hinds, E. Kendrick, D. J. L. Brett and P. R. Shearing, *Nat. Commun.*, (n.d.) (2020), 1 LINK <https://doi.org/10.1038/s41467-020-15811-x>
61. G. Zhang, X. Wei, X. Tang, J. Zhu and S. Chen, *Renew. Sustain. Energy Rev.*, 2021, **141**, (January), 110790 LINK <https://doi.org/10.1016/j.rser.2021.110790>
62. M. S. Pan, L. Su and K. Thornton, *Energy Environ. Sci.*, 2018, 860 LINK <https://doi.org/10.1039/c8ee00001h>

### <The Authors>

	<p>Drasti Patel is a PhD researcher at the Electrochemical Innovation Lab (EIL) at University College London (UCL). Her project is part sponsored by Johnson Matthey Battery Materials. Her research interests are in lithium-ion battery materials characterisation and failure assessment using X-ray CT imaging and calorimetry.</p>
	<p>Hamish Reid is currently a PhD researcher at the Electrochemical Innovation Laboratory (EIL) at University College London (UCL). Prior to joining the EIL, Hamish gained a Chemistry with a Year in Industry MChem at the University of Sheffield, where he spent a year working at The Dow Chemical Company. After graduating, Hamish worked at Faradion Ltd., researching cathode and anode materials for rechargeable sodium-ion batteries. His current research interests include X-ray imaging, battery safety, and degradation of high nickel content lithium-ion cathode materials. Hamish's doctorate work is partly funded by Johnson Matthey.</p>

	<p>Dr. Sarah Ball is currently Applications Technology Manager at Johnson Matthey Battery Materials. She has experience managing technical projects for Lithium Ion batteries and Hydrogen Fuel Cells, focussing on testing, evaluation and improvement of cathode and anode materials.</p>
	<p>Dan Brett is a professor of Chemical Engineering at UCL. His research interests lie in electrochemical energy conversion and storage, electrochemical sensors; electroanalysis, hybrid vehicles and micro-generation technologies. He is also active in modelling, instrumentation development, engineering design, device fabrication, materials development, and techno-economic analysis of electrochemical energy conversion technologies.</p>
	<p>Paul Shearing is a professor of Chemical Engineering at UCL and Royal Academy Engineering Chair in Emerging Battery technologies. His research interests lies in the design of electrochemical processes in devices including fuel cells, batteries, and electrochemical reactors. He is involved in a wide range of projects which includes the understanding and development of batteries, fuel cells and other electrochemical processes and leads the LiSTAR project and the SAFEBATT programme on battery safety, under the auspices of The Faraday Institution.</p>

**X-ray CT for Failure Mechanism Characterisation within Layered Pouch Cells**  
**Supplementary Information**



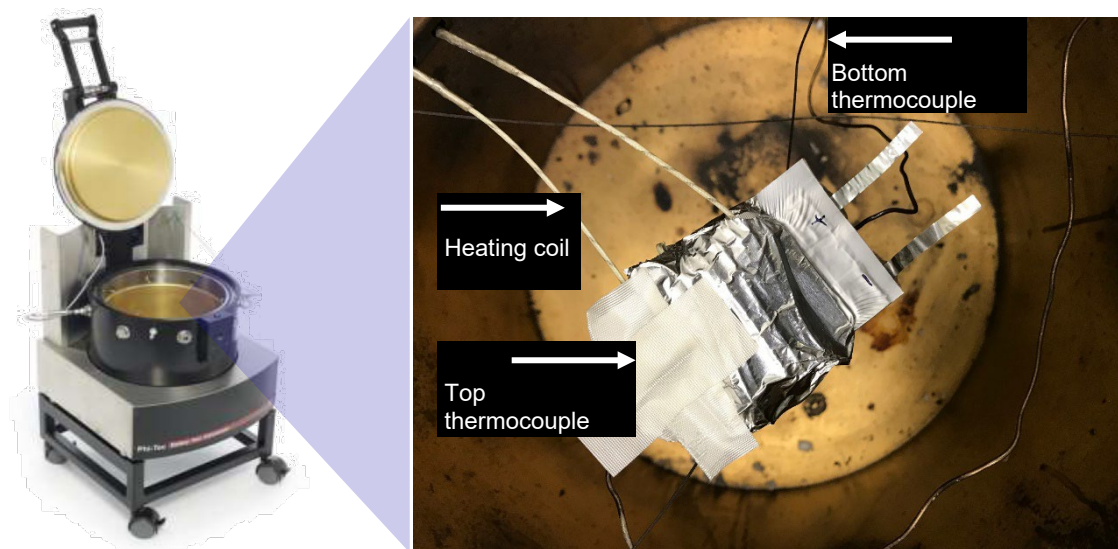


Figure S12 Photographs of (a) accelerating rate calorimeter (Phitec Battery Test Calorimeter, HEL Group, Herts., UK) and (b) set up of 1 Ah pouch cell (Cell 2) inside the calorimeter showing the heating coil and thermocouple positions.

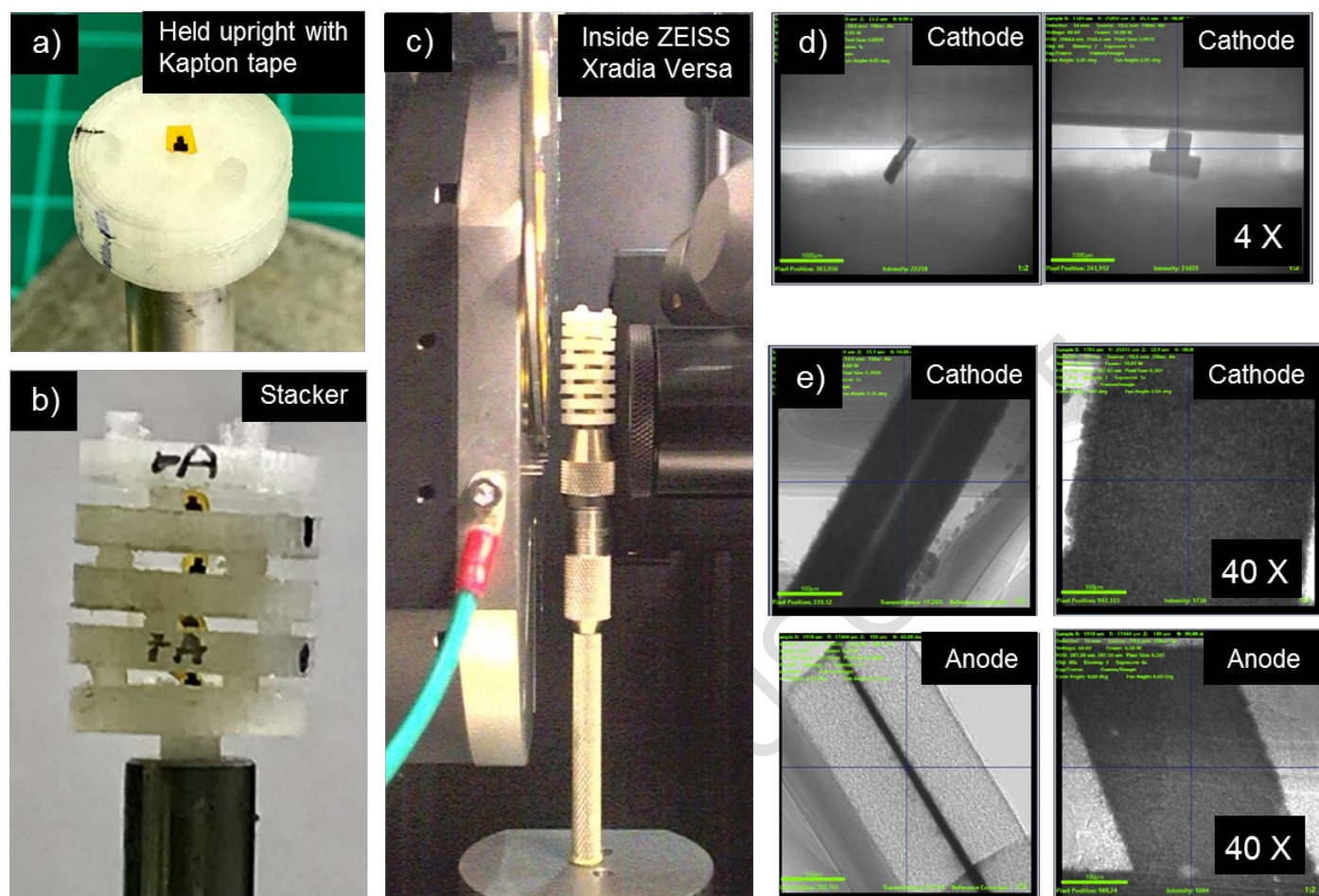


Figure S13 Photographs of (a) 0.4 x 0.4 mm sample placed upright in 3D printed holder, secured with Kapton tape, and (b) samples stacked, and (c) placed inside the ZEISS Xradia Versa 520. Radiographs in (d) show the sample within the FOV with the 4X objective lens and (e) shows the cathode and anode in the FOV with the 40 X objective lens.

## Cell after nail penetration

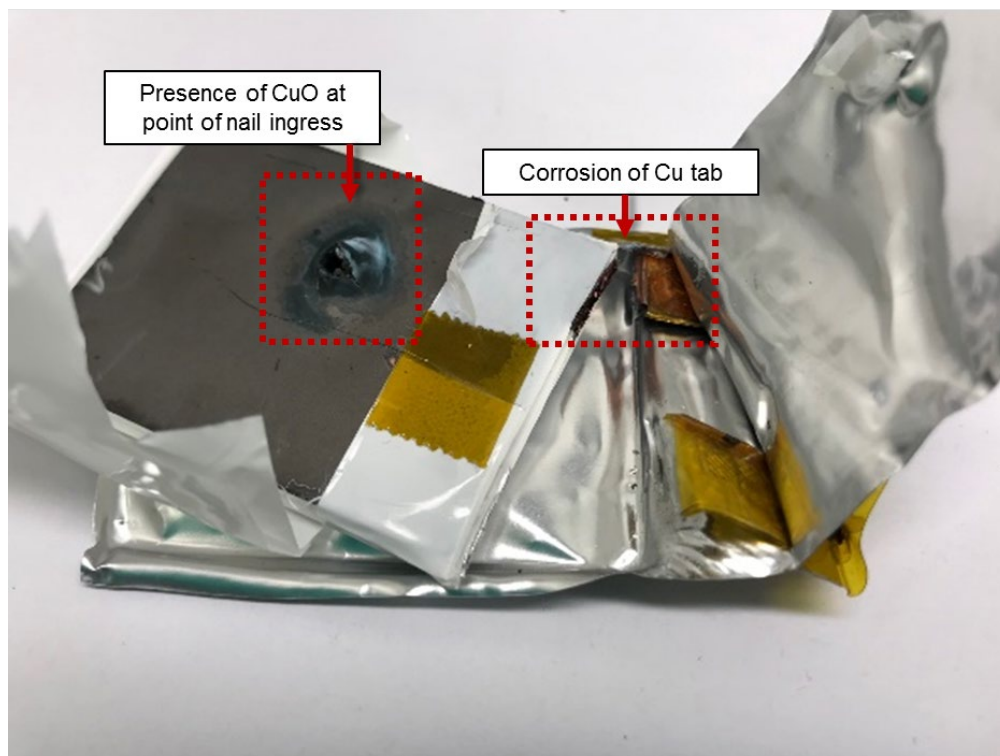


Figure S3 Photograph of the nail penetrated cell upon opening. The presence of CuO (green) is highlighted near the point of nail ingress as well as the corroded Cu tab.

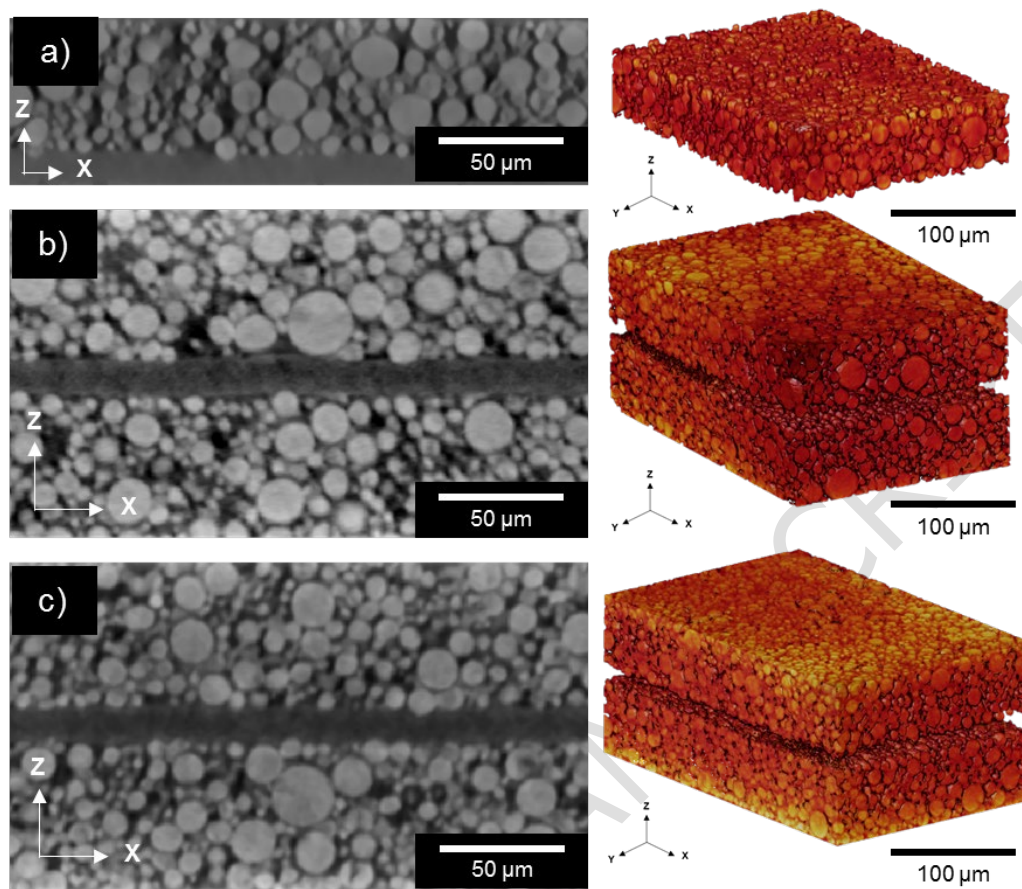


Figure S4 Orthoslice in the ZX plane and volume renderings of the (a) pristine, (b) thermally failed, and, (c) nail penetrated bulk cathode layers taken from scans 7, 9 and 11 with corresponding voxel sizes of 0.181, 0.387 and 0.387 μm.



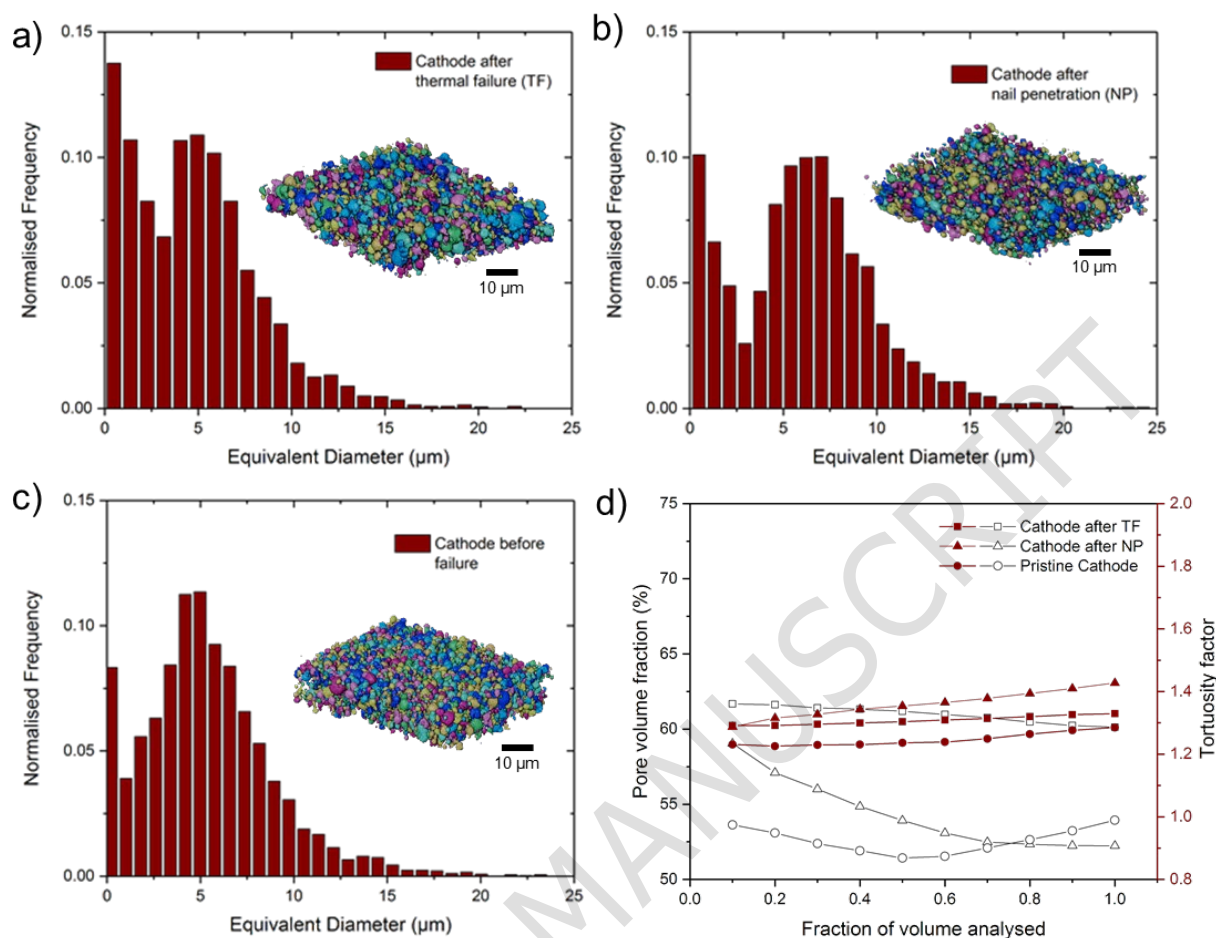


Figure S5 Particle size distributions for the (a) pristine, (b) thermally failed, and, (c) nail penetrated bulk cathode layer samples. A representative volume analysis of the pore volume fraction and tortuosity factor as a function of the fraction of the volume analysed is shown in (d).

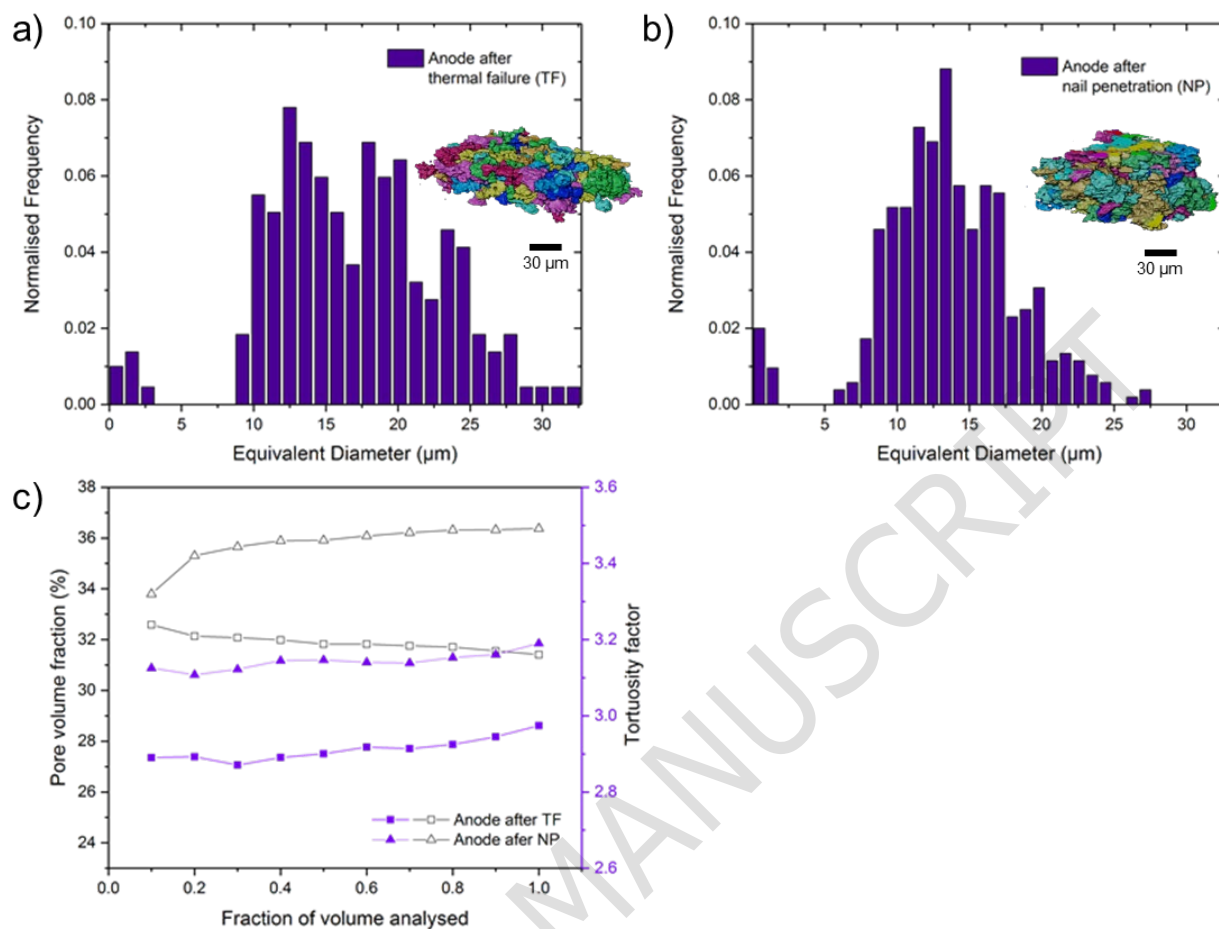


Figure S6 Particle size distributions for the (a) thermally failed, and, (b) nail penetrated bulk anode layer samples taken from the centre of the cell 2 and 3, respectively. A representative volume analysis of the pore volume fraction and tortuosity factor as a function of the fraction of the volume analysed is shown in (c).

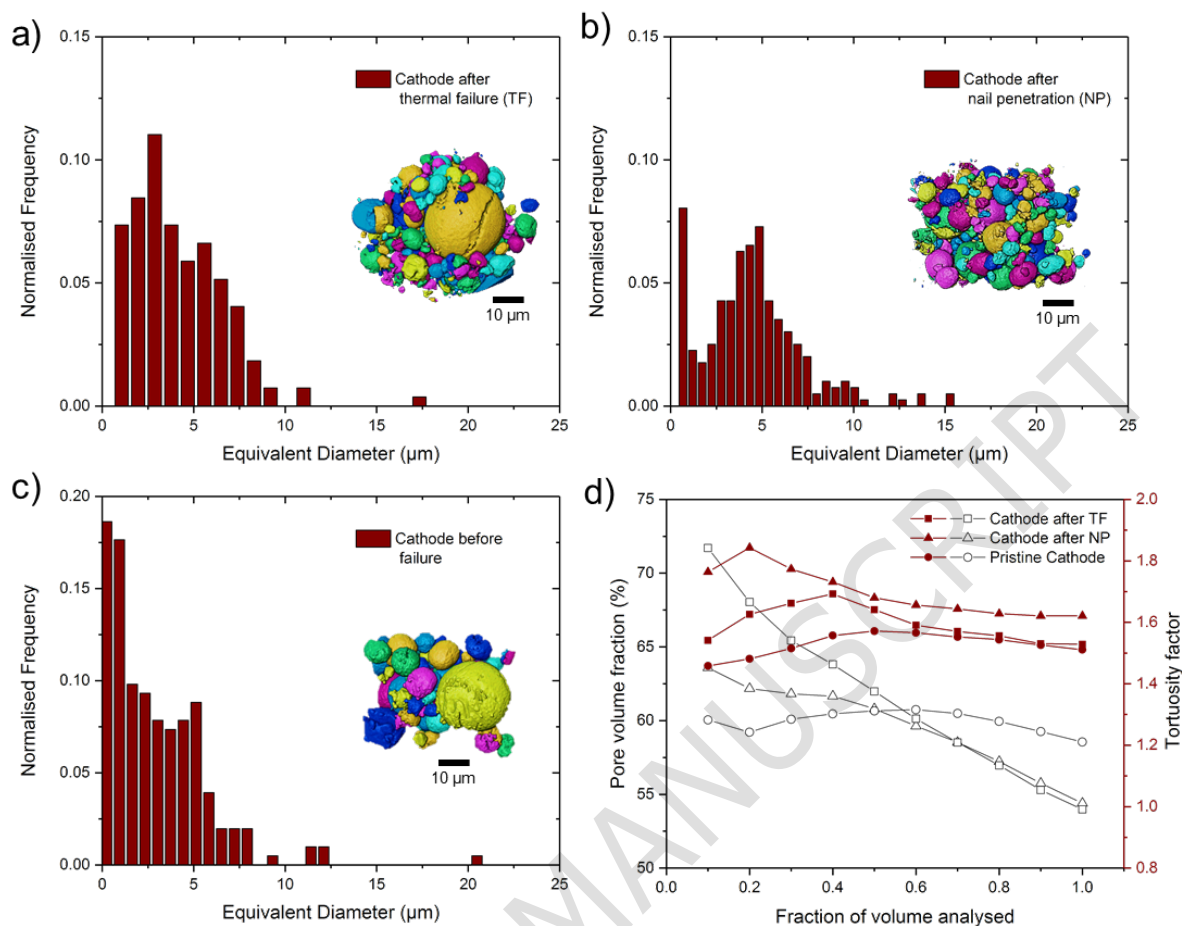


Figure S7 Particle size distributions for the (a) pristine, (b) thermally failed, and, (c) nail penetrated particles. A representative volume analysis of the pore volume fraction and tortuosity factor as a function of the fraction of the volume analysed is shown in (d).

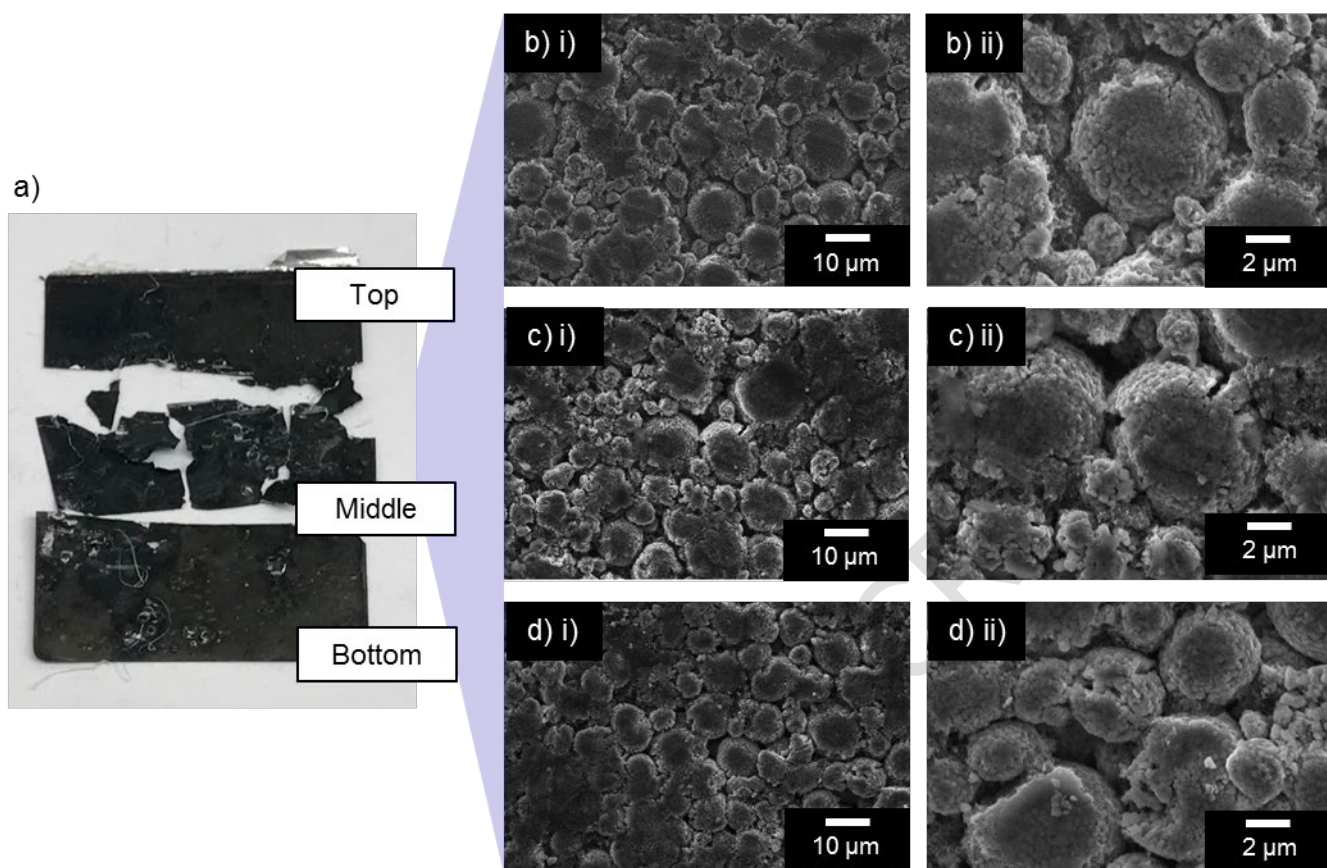


Figure S8 SEM micrographs taken at the (b)(i– ii) top, (c)(i– ii) middle, and, (d)(i– ii) bottom, at different magnifications across the cathode layer of the nail penetrated cell.



Table S1 Summary of voxel sizes, in  $\mu\text{m}$ , achieved for all scans.

Imaging instrument	FOV	Cell 1: Pristine cell and materials (no failure mode)			Cell 2: External heating by accelerating rate calorimetry (ARC)			Cell 3: Internal short circuit by nail penetration			
		Whole cell	Anode	Cathode	Whole cell	Anode	Cathode	Whole cell	Anode	Cathode	
Nikon XT 255	X	31.7 (#1)			33.6 (#2)			27.8 (#3)			Non-invasive / whole cell
ZEISS Xradia 520 Versa (4 X obj. lens)	300 – 400 0	1.83 (#4)			2.00 (#5)			1.70 (#6)			
ZEISS Xradia 520 Versa (40 X obj. lens)	384			0.181 (#7)	0.387 (#8)	0.387 (#9)		0.387 (#10)	0.387 (#11)		Invasive
ZEISS Xradia 810 Ultra (LFOV)	64			0.0631 (#12)		0.126 (#13)			0.126 (#14)		

ZEISS		—	0.035	0.03	0.035	0.03	0.035
SEM	N/A		—	5	—	5	—
EVO MA			0.090	0.09	—	0.09	—
10				0	0.090	0	0.090

Table S2 Summary of parameters extracted from the invasive (bulk electrode layer and particle morphology) scans.

		Pristine cathode		Cathode after Thermal failure (TF)*		Cathode after Nail penetration (NP)**		Anode after TF*	Anode after NP**
		Versa (#7)	Ultra (#12)	Versa (#9)	Ultra (#13)	Versa (#11)	Ultra (#14)	Versa (#8)	Versa (#10)
Imagine instrument and (#scan number)		Versa (#7)	Ultra (#12)	Versa (#9)	Ultra (#13)	Versa (#11)	Ultra (#14)	Versa (#8)	Versa (#10)
Sample type/feature of interest	of	(I)	(II)	(I)	(II)	(I)	(II)	(I)	(I)
Voxel size (μm)		0.181	0.0631	0.387	0.126	0.387	0.126	0.387	0.387
Bounding box dimension (total voxels)	box (total voxels)	326 x 1475 x 1029	421 x 488 x 542	516 x 794 x 129	339 x 352 x 368	129 x 794 x 516	307 x 353 x 485	646 x 559 x 154	491 x 605 x 169
Mean particle diameter (μm)	particle diameter (μm)	5.39 ± 0.65	2.93 ± 0.51	4.76 ± 0.64	4.43 ± 0.50	6.10 ± 0.70	4.47 ± 0.42	16.99 ± 1.01	13.59 ± 0.76
Min. particle diameter (μm)	particle diameter (μm)	0.22	0.24	0.48	1.06	0.4	0.68	0.48	0.48
Max. particle diameter (μm)	particle diameter (μm)	23.20	20.49	26.40	26.38	24.26	15.27	32.16	27.15
Particle volume fraction	volume fraction	0.46	0.42	0.40	0.46	0.48	0.46	0.69	0.64
Tortuosity		1.29	1.51	1.33	1.53	1.43	1.62	2.97	3.19
Surface area per volume (μm <sup>-1</sup> )	Surface area per volume (μm <sup>-1</sup> )	0.478	0.429	0.408	0.572	0.490	0.764	0.654	0.660

\*Extracted from Cell 2, \*\*Extracted from Cell 3  
(I) Bulk electrode layer via micro-CT, (II) Particle via nano-CT

ACCEPTED MANUSCRIPT